Wind and Structures, *Vol. 23, No. 4 (2016) 313-350*
DOI: http://dx.doi.org/10.12989/was.2016.23.4.313

Evaluation of wind loads and wind induced responses of a super-tall building by large eddy simulation

C.L. Lu[1], Q.S. Li[*2], S.H. Huang[3], Alex Y. Tuan[4], L.H. Zhi[1] and Sheng-chung Su[5]

[1]*College of Civil Engineering, Hunan University, Changsha 410082, China*
[2]*Department of Architecture and Civil Engineering, City University of Hong Kong, Kowloon, Hong Kong*
[3]*School of Engineering Science, University of Science and Technology of China,Hefei, 230026, China*
[4]*Department of Civil Engineering, Tamkang University, Tamsui, Taiwan*
[5]*Central Weather Bureau, Taipei, Taiwan*

(Received January 5, 2015, Revised July 15, 2016, Accepted July 19, 2016)

Abstract. Taipei 101 Tower, which has 101 stories with height of 508 m, is located in Taipei where typhoons and earthquakes commonly occur. It is currently the second tallest building in the world. Therefore, the dynamic performance of the super-tall building under strong wind actions requires particular attentions. In this study, Large Eddy Simulation (LES) integrated with a new inflow turbulence generator and a new sub-grid scale (SGS) model was conducted to simulate the wind loads on the super-tall building. Three-dimensional finite element model of Taipei 101 Tower was established and used to evaluate the wind-induced responses of the high-rise structure based on the simulated wind forces. The numerical results were found to be consistent with those measured from a vibration monitoring system installed in the building. Furthermore, the equivalent static wind loads on the building, which were computed by the time-domain and frequency-domain analysis, respectively, were in satisfactory agreement with available wind tunnel testing results. It has been demonstrated through the validation studies that the numerical framework presented in this paper, including the recommended SGS model, the inflow turbulence generation technique and associated numerical treatments, is a useful tool for evaluation of the wind loads and wind-induced responses of tall buildings.

Keywords: tall building; computational fluid dynamics (CFD); large eddy simulation (LES); finite element method (FEM); wind load; wind-induced response; full-scale measurement; wind tunnel test

1. Introduction

Recent trends towards constructing increasingly slender and taller buildings, with higher strength materials and lighter structural systems, have resulted in a new generation of wind-sensitive buildings. Such structures are usually slender, lightweight, and flexible and have low damping and natural frequencies, which are sensitive to wind loads and undergo excessive wind-induced vibrations, causing discomforts to occupants. Taipei 101 Tower as an example of this kind of structure, rising 508 m above the city of Taipei, earns the title of the second tallest building in the world. Its dynamic responses to wind, earthquakes and other extraordinary loads

*Corresponding author, Professor, E-mail: bcqsli@cityu.edu.hk

http://www.techno-press.org/?journal=was&subpage=8 ISSN: 1226-6116 (Print), 1598-6225 (Online)

are of great concern. As Taiwan is located in one of the most active typhoon-generating areas in the world, typhoon winds could excite Taipei 101 Tower with forces much greater than those normally experienced by common tall buildings. The great height of the building and the extreme environmental conditions, not surprisingly, presented one of the greatest challenges for structural engineers. These features require a detailed study of the structural performance under wind actions.

At present, there are mainly three approaches to pre-estimate the design wind loads and wind induced response of structures, including: full-scale measurements, wind tunnel tests and numerical simulations based on Computational Fluid Dynamics (CFD). Each method has, of course, advantages and limitations, and to some extent, they are complementary.

Full-scale measurement can obtain the first hand data of wind loads and wind-induced responses of a prototype structure. In the last two decades, with the development of data acquisition techniques, a number of full-scale measurements of wind or seismic effects on tall buildings have been made throughout the world (Li *et al.* 2005, Li *et al.* 2008, Jeary 1986, Ohkuma 1991, Littler and Ellis 1992, Tracy *et al*. 2007, Tracy and Pirnia 2007), including on ten super-tall buildings in Hong Kong and Mainland China by the City University of Hong Kong ((Li *et al.* 2005, Li *et al.* 2008) and the Chicago full-scale monitoring project performed by Notre Dame University and the University of Western Ontario to validate the performance of four tall buildings in Chicago (Tracy *et al*. 2007, Tracy and Pirnia 2007). However, field measurements can only be applicable to existing structures. For the wind-resistant design of future super-tall buildings which are not fully covered by current design codes or standards, it is required to adopt wind tunnel tests or numerical approaches for determinations of design wind loads.

Wind tunnel testing is a relatively mature technology in wind engineering and has become the most conventional way in estimating wind effects on buildings and structures. However, there are several problems involved in wind tunnel tests. Firstly, wind tunnel testing is usually conducted with a scaled model (1/100~1/500) of a prototype building, resulting in the Reynolds numbers of model tests are much smaller than those of prototype buildings. Comparisons between the wind tunnel test results and full-scale measurements of surface pressures on the Texas Technical University (TTU) building showed that the mean pressure coefficient distributions were in good agreement but the local fluctuating pressure coefficients, and especially the peak pressure coefficients, significantly differed from those measured from the prototype building (Cochran and Cermak 1992, Okada and Ha 1992, Li and Melbourne 1996). This may be attributed to several reasons including the differences in Reynolds numbers between the model tests and the field measurements (Cheung *et al*. 1997). Secondly, it is difficult to reproduce the exact field conditions, such as incident turbulence and terrain characteristics in wind tunnel tests. It has been reported that the real structures of atmospheric turbulence and those simulated in wind tunnels are somewhat different (Li *et al.* 2009, 2010).

Computational wind engineering (CWE) as a branch of CFD has been developed rapidly over the last two decades to evaluate wind effects on structures numerically, offering an alternative technique for practical applications. CFD based numerical techniques are particularly effective for CWE applications in the following aspects: it can clarify the process and mechanism of non-periodic and localized phenomena due to its abundant detailed data, such as flow field information and pressure distributions on the surfaces of a building.

However, as noted by Stathopoulos (1997), Murakami (1998), Baker (2007), Huang *et al*. (2010) and others, there are several problems with the practical use of LES in wind engineering. One of the most key limitations of CFD is high Reynolds number turbulence simulation for

bluff-body flows. In fact, high Reynolds number turbulence simulation to ensure generating a flow field as an inflow boundary condition (inflow turbulence) to be consistent with the actual characteristics of wind flows and atmospheric turbulence is one of the most difficult problems yet to be solved in the turbulence research field.

The inflow turbulence generated by numerical simulations is very important in determining wind forces and dynamic response of buildings, which is a main factor of influencing the accuracy and reliability of CFD numerical simulations as a predictor of wind effects on structures. The approaching flow simulated in a computational domain should have inherent characteristics of actual atmospheric flows. Currently, there are two kinds of inflow turbulence generation methods. The first is numerically simulating turbulent flows in an auxiliary computational domain. Nozawa and Tamura (2002, 2005) used a roughness block arrangement based on roughness density and empirical formula for rough-wall friction to form the inflow conditions in their studies. The other method is statistically generating an inflow turbulent field by an artificial numerical model. Recently, a general inflow turbulence generator for LES has been established by Huang *et al*. (2010), which belongs to the second kind of method and was developed based on the discretizing and synthesizing of the random flow generation (DSRFG) technique. The newly developed method has been proved to be able to generate a fluctuating turbulent flow field satisfying desired spectra and spatial correlations including inhomogeneity and anisotropy as well as prescribed profiles of turbulence intensity and turbulence integral length scale. In addition, the DSRFG-based method has a built-in divergence-free mechanism in random velocity generation. Hence, no velocity correction and preliminary storage for time-sequential data are needed. Due to the above mentioned advantages, the new method is adopted in this study for generation of inflow turbulent field.

Since the pioneering work of Smagorinsky, after about 48 years of extensive research works, the development of the sub-grid scale (SGS) models of LES has gone through the following three stages: earlier algebraic eddy viscosity models, one-equation eddy viscosity models and two-equation eddy viscosity models. Huang and Li (2010) summarized the advantages and limitations of the three classes of the SGS models and pointed out that there are two contradictions limiting their applications in engineering practices---the contradiction of the low-order discretization, unstructured grid with the test-filtering operation and the contradiction of the non-equilibrium characteristics (in high Reynolds number flows and coarse grid situations) with the local equilibrium assumption involved in the algebraic SGS models. A new SGS model combining both the advantages of a dynamic one-equation SGS model (Kajishima and Nomachi 2006) and the wall-adapting local eddy viscosity model (Nicoud and Ducros 1999) was developed by Huang and Li (2010). It was demonstrated by Huang and Li (2010) that the new SGS model is a useful tool for wind engineering applications.

In this paper, the effective inflow turbulence generation method (Huang *et al*. 2010) and the new SGS model (Huang and Li 2010) are applied to the LES of wind effects on Taipei 101 Tower. Unlike the majority of the past studies on LES of wind effects on tall buildings, scaled building models were usually considered in their computations. The present LES is conducted for full-scale sizes of the target tall building with Reynolds number greater than 10^8. The simulated dynamics wind loads on the super-tall building are then used as inputs to the finite element model of Taipei 101 Tower. The dynamic analysis of the high-rise structure is conducted. The calculated wind-induced dynamic responses of the tall building are compared with those obtained from the field measurements and wind tunnel test results. Furthermore, the equivalent static wind loads on the tall building are calculated by the time-domain method and frequency-domain method,

respectively, which are compared with available wind tunnel test results. The validation studies show good agreement between the computational results and the measured data, thus verifying the present numerical simulation framework based on the DSRFG approach and the new SGS model is an effective tool for predicting the wind loads and wind-induced vibrations of super-tall buildings.

2 Introduction of Taipei 101 Tower

Taipei 101 Tower, a 508-meter high office tower with a 101-storey superstructure and a 5-storey basement, is located in the east district of downtown Taipei City. An elevation view of the tall building is shown in Fig. 1. The structure is symmetrical with a 62.4 m by 62.4 m square footprint (Research Institute of Building & Construction 1999). Fig. 2 shows an elevation view and the locations of the belt trusses.

Fig. 1 Elevation view of Taipei 101 Tower

A vibration monitoring system has been installed in Taipei 101 Tower, including two major parts: the data acquisition and storage platform, and the sensor subsystem. The sensor subsystem includes 30 accelerometers located at the -5th (basement), 1st, 36th, 60th, 89th and 101st floor, as shown in Fig. 3. Though analyzing the data measured from these sensors, the structural acceleration responses and dynamic characteristics (such as natural frequencies, mode shapes, and damping ratios) of the tall building can be obtained. To measure the rotational accelerations of the tower, four accelerometers were placed at two locations on a floor along the two major axes (X direction and Y direction) of this building, as shown in Fig. 4.

The primary objective of the present investigation is to evaluate the wind effects on tall buildings through full-scale size LES based on the DSRFG approach and new SGS model developed by the authors. Taipei 101 Tower is a very good candidate for this study, by being the second tallest building in the world and especially the vibration monitoring system has been installed in the building. This will allow us to compare the simulated results with the field measurements for verification of the newly developed computational approaches. The acceleration data selected for the validation study were continuously acquired and digitized at 200 Hz from the monitoring system during three typhoons and an earthquake excitation from August 2005 to May 2008.

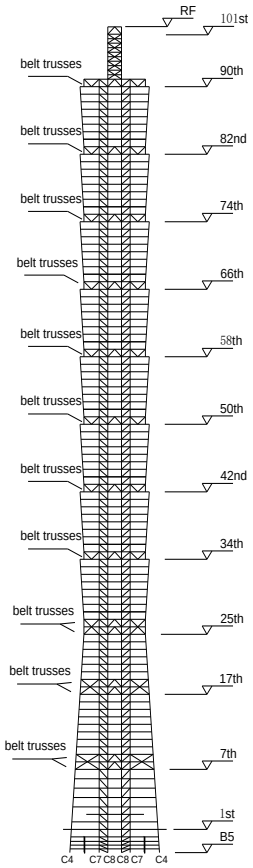

Fig. 2 Elevation view of the structural system

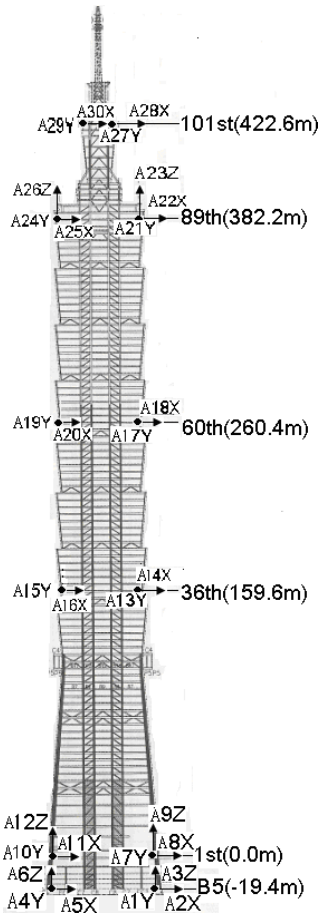

Fig. 3 Locations of the installed accelerometers

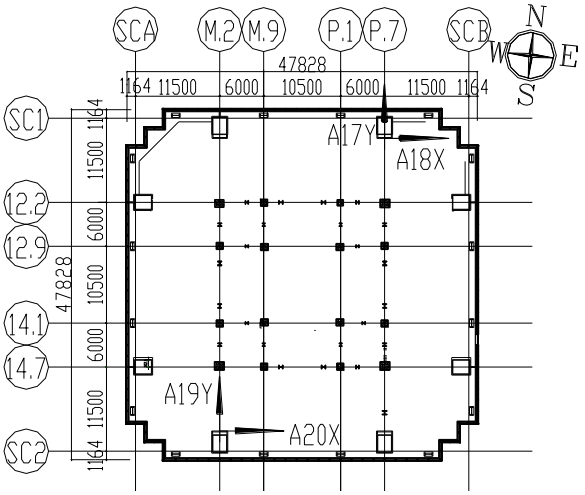

Fig. 4 Accelerometer arrangement on the 60th floor

3. Numerical simulation models and methods

In the numerical study, the commercial CFD software FLUENT together with the DSRFG approach and the new SGS model recently developed by Huang *et al.* (2010) and Huang and Li (2010) were utilized to simulate three-dimensional (3D) unsteady flow field around Taipei 101 Tower.

The computational domain shown in Fig. 5 was chosen to cover 33 D_b (D_b is the width of the building) in streamwise (X) direction (-6<x/ D_b <32), 17B in lateral or normal (Y) direction (-8<y/ D_b <8) and 2 H (H is the building height) in vertical (Z) direction. The blockage ratio of the building sizes in the computational domain is less than 3%.

The mesh arrangement for the target building (see Fig. 6(a)) is a nesting style with hybrid mesh as discussed in (Huang *et al.* 2007). For the zones in the nesting rectangular cylinder, unstructured mesh was generated while for the regions outside the nesting rectangular cylinder, the structured mesh was produced. This arrangement makes it easier to generate relative fine mesh in the neighborhood of the building surfaces (0.01 m for the first wall cell height), while keeping the mesh in the zones far away from the building surfaces unchanged or in a proper coarser manner (the meshes' grid stretching ratio in wake region is restricted to be less than 1.05 for reducing the difference of cut-off wave number between neighboring grids in the LES). Totally 3,209,050 3D grids were generated for the present simulations. The mesh quality measured by skewness of equisize angle is generally shown in Fig 6(b), the maximum of skewness is about 0.896, which is in a proper range of unstructured mesh.

To fully account for the unsteadiness of the wind loads on the tall building, the LES is conducted while the new dynamic SGS model proposed by Huang and Li (2010) is adopted in this study.

The SGS kinetic energy is defined as $k_{sgs} = \frac{1}{2}(\overline{U_k^2} - \overline{U}_k^2)$, which is obtained by contracting the subgrid-scale stress in $\tau_{ij} = \rho\overline{U_i U_j} - \rho\overline{U}_i\overline{U}_j$. The SGS eddy viscosity, μ_t, is computed using k_{sgs} as $\mu_t = C_k k_{sgs}^{1/2}\Delta_f$, where Δ_f is the filter-size computed from $\Delta_f \equiv V^{1/3}$. The subgrid-scale stress can then be expressed as $\tau_{ij} = \frac{2}{3}k_{sgs}\delta_{i,j} - 2\mu_t\overline{S}_{i,j}$, while k_{sgs} is obtained by solving its transport equation

$$\frac{\partial k_{sgs}}{\partial t} + \frac{\partial \overline{U}_j k_{sgs}}{\partial x_j} = -\tau_{ij}\frac{\partial \overline{U}_i}{\partial x_j} - C_\varepsilon \frac{k_{sgs}^{3/2}}{\Delta_f} + \frac{\partial}{\partial x_j}\left(\frac{\mu_t}{\sigma_k}\frac{\partial k_{sgs}}{\partial x_j}\right) \tag{1}$$

In the above equation, the model constants, C_k and C_ε are determined dynamically (Kim and Menon 1997). σ_k is 1.0.

The inlet mean wind speed profile is described by a power law function as follows

$$\frac{U}{U_{10}} = \left(\frac{Z}{Z_{10}}\right)^a \tag{2}$$

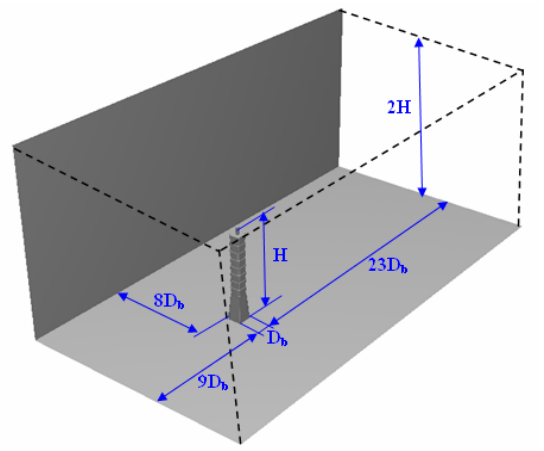

Fig. 5 Computational domain and boundary conditions

where a is the exponent of the mean wind speed profile and U_{10} is the mean wind speed at height of 10m. According to the statistical wind climate model and the typhoon simulation results based on local wind speed measurements taken at Taipei Sungshan Airport, a 10-miniute mean wind speed of 43.27 m/s at the 10m height above ground and a=0.15 are used in the present study, which are consistent with the design wind speed with 50 years return period as stipulated in the Taiwan Building Code (1999).

There is lack of sufficient field measurement information on the variations of turbulence parameters from ground to a height of 600 m, especially under high-wind conditions such as strong typhoons. Shiau (2000) conducted field measurements of strong winds (typhoons) at 26 m height on an observation tower located in Keelung harbor, about 20 km north of Taipei. The measured data showed the longitudinal turbulence intensity changed in the range of 0.18 to 0.23 and the longitudinal turbulence integral length scale varied from 40 m to 200 m in the wind speed range from 27 m/s to 45 m/s. Li *et al.* (2005), Li *et al*. (2008) made field measurements of wind velocity atop Central Plaza Tower (374 m) in Hong Kong and Di Wang Tower (384 m) in Shenzhen during typhoons. Their measured turbulence intensity ranged from 0.1 to 0.4 and the integral length scale changed from 171 m to 600 m in the wind speed range from 5 m/s to 25 m/s. Based on these field data, the inflow profiles of turbulence intensity and integral length scale are determined, as shown in Fig. 7.

The inflow turbulence is generated by the DSRFG method Huang *et al*. (2010) which is briefly described below

$$\mathbf{u}(\mathbf{x},t)=\sum_{m=k_0}^{k_{max}}\mathbf{u}_m(\mathbf{x},t)=\sum_{m=k_0}^{k_{max}}\sum_{n=1}^{N}[\mathbf{p}^{m,n}\cos(\tilde{\mathbf{k}}^{m,n}\cdot\tilde{\mathbf{x}}+\omega_{m,n}t)+\mathbf{q}^{m,n}\sin(\tilde{\mathbf{k}}^{m,n}\cdot\tilde{\mathbf{x}}+\omega_{m,n}t)] \quad (3)$$

where $\mathbf{p}^{m,n}$ and $\mathbf{q}^{m,n}$ are determined as follows

$$\mathbf{p}^{m,n} = \frac{\varsigma \times \mathbf{k}^{m,n}}{\left|\varsigma \times \mathbf{k}^{m,n}\right|}\sqrt{a\frac{4E(k_m)}{N}} \tag{4}$$

$$\mathbf{q}^{\mathrm{m,n}} = \frac{\xi \times \mathbf{k}^{\mathrm{m,n}}}{\left|\xi \times \mathbf{k}^{\mathrm{m,n}}\right|}\sqrt{(1-\mathrm{a})\frac{4\mathrm{E}(\mathrm{k_m})}{\mathrm{N}}} \tag{5}$$

$$\tilde{\mathbf{x}} = \frac{\mathbf{x}}{L_s} \tag{6}$$

$$\tilde{\mathbf{k}}^{m,n} = \frac{\mathbf{k}^{m,n}}{k_0},\ \left|\mathbf{k}^{m,n}\right| = k_m \tag{7}$$

$$\omega_{\mathrm{m,n}} \in \mathrm{N}(0,2\pi \mathrm{f_m}), \mathrm{f_m} = \mathrm{k_m U_{avg}} \tag{8}$$

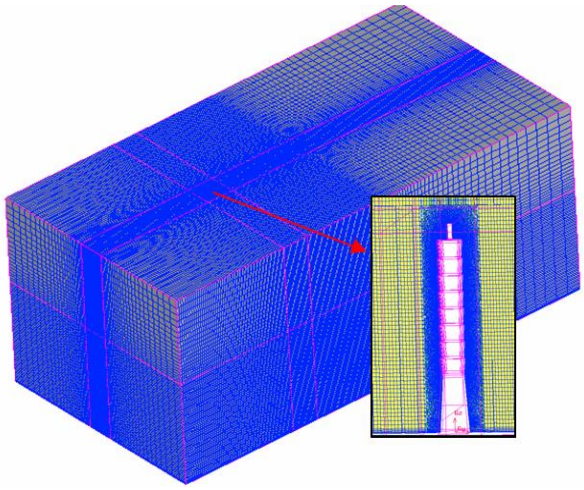

(a)

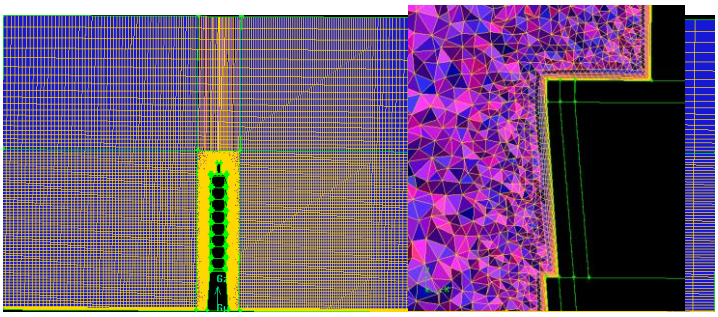

(b)

Fig. 6 Computational mesh arrangement

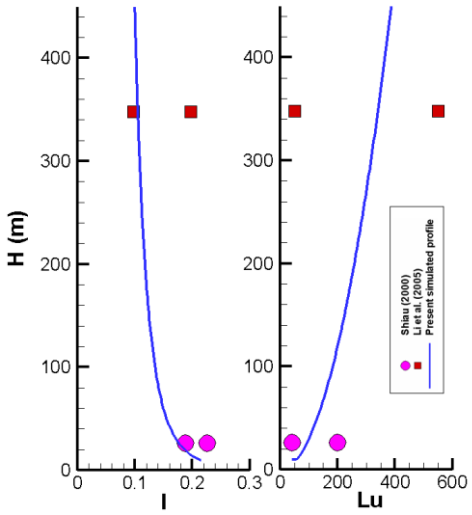

Fig. 7 Inflow turbulence profiles

where $\mathbf{x}$ is vector of space location, ς and ξ are the vector form of ς_i^n and ξ_i^n, respectively; f is the wave frequency and U_{avg} is mean velocity; L_s is a length scale of turbulence and is used as a scaling factor for adjustment of spatial correlation. It has been proved that the above inflow turbulence generator can strictly guarantee divergence-free conditions without any additional improving step and is able to synthetically generate inflows satisfying the prescribed spatial anisotropy and spatial correlation conditions as well as the target profiles of turbulence parameters (Huang *et al*. 2010). Fig. 8 shows an instantaneous velocity field at the inflow boundary generated by the DSRFG method. Clearly, many vortices which are consistent with the actual characteristics of atmospheric wind flows are observed at the inflow boundary generated by the DSRFG method. The power spectral density (PSD) of the generated wind velocity fluctuations is plotted in Fig. 9 with comparison with the target spectrum (von-Karman spectrum). It is evident that the PSD of the generated wind velocity fluctuations agree well with the von-Karman spectrum.

The new SGS model and the inflow condition proposed and developed by Huang and Li (2010) and Huang *et al*. (2010) were implemented as a User Defined Function (UDF) library, which was integrated into the FLUENT code by programming technique of user defined scalar and function hooks.

Besides, for full scale high-Reynolds number LES, to resolve laminar sublayer near building walls is extremely expensive in computational cost. Hence, the first wall cell height with 0.01 m is adopted in the present investigation, resulting in averaged 60 y+ on the building wall boundary. Werner-Wengle wall functions are used to compute wall shear stress based on analytical integration of the power-law near-wall velocity distribution.

Wind flow motion concerned in wind engineering applications is relatively slow and can be considered as incompressible flow in general. In this study, all the discretized equations are solved in a segregated manner with the Pressure Implicit with Splitting of Operators (PISO) algorithm.

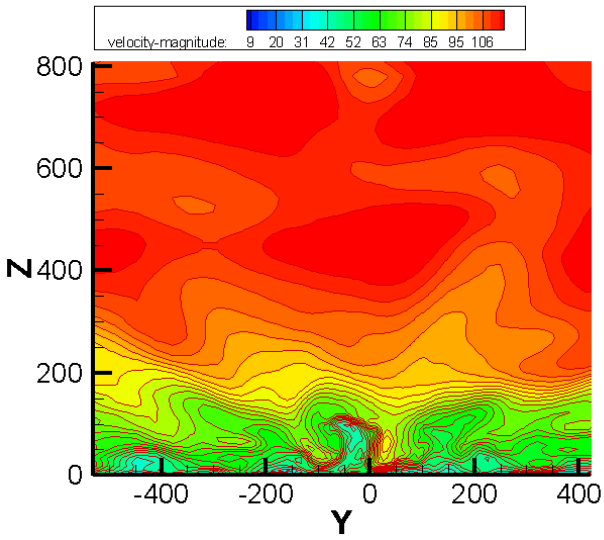

Fig. 8 Instantaneous velocity field at the inflow boundary generated by the DSRFG method

Second order discretization schemes are used for time and spatial discretization. Body Central Differencing (BCD) is used for momentum discretization. The time derivative is discretized using the second order backward differences and the spatial discretization is treated implicitly. The numerical approximation of gradients is by Green-Gauss cell based method.

The computations were performed on a high-performance cluster with 32CPUs. With consideration of the balance between the accuracy of the LES and computational expenses, 0.05 seconds per time step was adopted in the present computation. Totally, 16,000 time steps were taken to obtain the results of the turbulent flow field. The statistical averaging of the flow field was taken for the last 11,000 steps (550 seconds of physical time).

The computational expense for the LES is summarized here: memory usage 12GB, CPU time 733 hours with each time step being about 60 seconds (5 sub-iterations).

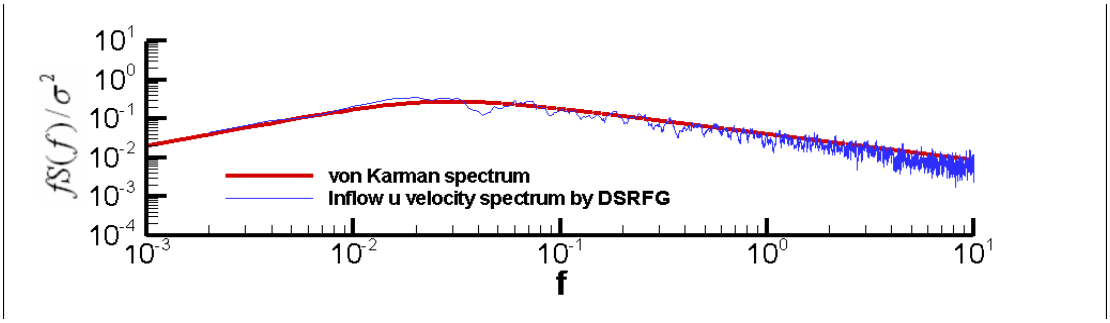

Fig. 9 Velocity spectrum generated by DSRFG

4. Flow field investigation

Typical flow patterns of winds around a building generally include horseshoe vortices, separations at building corners and leading edges, flow recirculation zones, shear layers and wake flows, etc. The instantaneous and mean velocity contours predicted by the present numerical simulation are shown in Figs. 10(a) and 10(b), respectively. The features of a typical bluff-body flow field addressed above such as separation flows at the frontal corners and windward top wall of the building, vortex shedding, shear layers and wake flows were properly reproduced by the inflow turbulence generator (DSRFG).

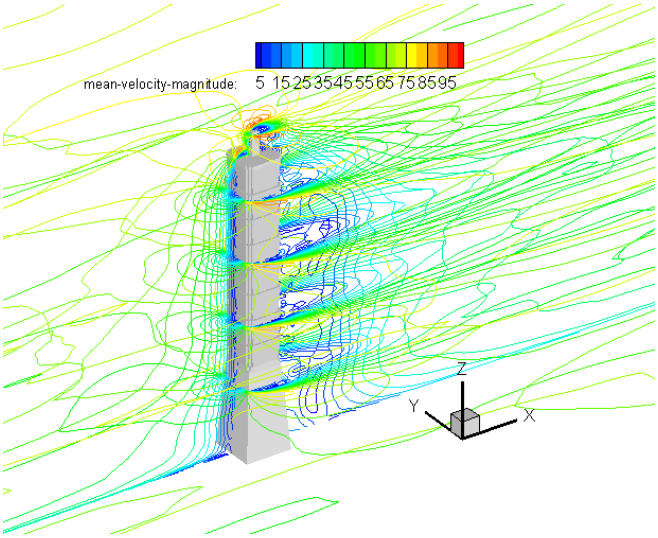

(a) Mean velocity contours

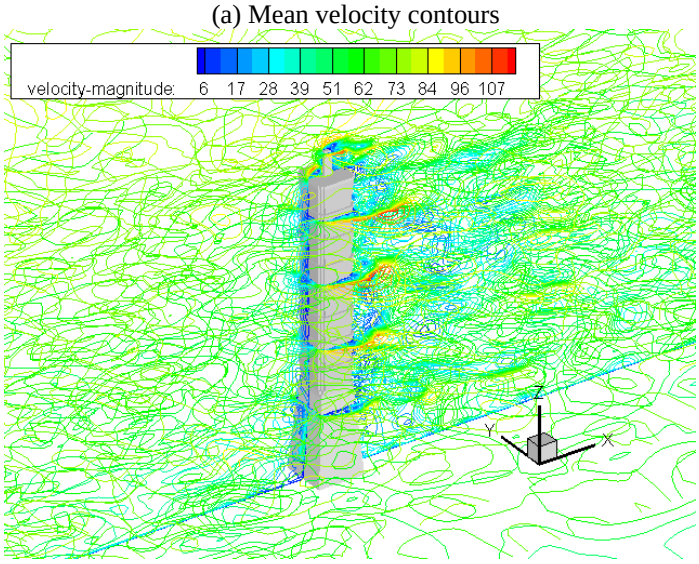

(b) Instantaneous velocity contours

Fig. 10 Instantaneous velocity contours around Taipei 101 Tower

5. Characteristics of wind forces

As the main interest of this study is to predict the wind effects on super-tall building by LES, it is required to determine the wind-induced forces on the surfaces of the tall building at the first stage.

The time-histories of the wind forces along the two main body axes (X and Y directions), Fx, Fy and torsional moments Mz on 51 layers (one layer covers two stories) on the building were determined by integrating the simulated wind-induced pressures with their associated tributary areas at each time step during the LES. The overall wind loads on the building were calculated by integrating the wind forces on the 51 layers.

The time-histories of the overall wind forces (drag, F_D), (lift, F_L), (torsional moment, M) are shown in Fig. 11. It can be seen from the figure that the fluctuation patterns of the forces are irregular, indicating that random wind actions on the building were predicted by the LES.

5.1 Spectral analysis of the wind loads

The power spectral densities (PSD) of the overall wind forces and the accelerations recorded at the basement of the building during "Wenchuan" earthquake occurred on May 12, 2008 are shown in Figs. 12 and 13, respectively. It is interesting to note that the energy distributions of the wind forces on the super-tall building and the long-distance earthquake -induced ground accelerations all mainly concentrated in 0-2 Hz. This is because most of the high-frequency components of the earthquake wave would have been filtered out by the earth during the long-distance (about 1,890 km) travelling from Wenchuan to Taipei. This phenomenon implies that a long-distance earthquake excitation on a super-tall building such as Taipei 101 Tower is, to some extents, similar to the wind actions on the high-rise building.

The wind force spectra in along-wind and across-wind directions as well as torsional motion at layers 50, 40, 30 and 20 obtained by the LES are shown in Figs.14-16.

Fig. 14 shows that the along-wind force spectra are similar to a typical longitudinal wind velocity spectrum with a wide band. This figure shows the magnitudes of the PSD of the along-wind forces near the spectral peak decrease with the increases in the building height. This may be caused by the down flows from the windward wall of the building. Except in this frequency band, the variation of the spectral magnitude with elevation is not obvious.

Fig. 15 presents the wind force spectra in across-wind direction. There is a peak in each spectrum, which is caused by vortex shedding. This illustrates that the across-wind forces are mainly caused by vortex shedding. Along the building elevation, the variation of the across-wind force spectra near the spectral peak is not obvious. However, in the higher frequency band, the PSD curves increase with the elevation. A reasonable explanation for this phenomenon is: at higher elevations, 3D flows and higher velocities caused relatively high pressures on the sidewalls, which contribute to the high-frequency portion of the local force spectra in the across-wind direction.

The torsional moment spectra are shown in Fig. 16. There is also a peak in each spectrum, which is near that of the across-wind force spectra, indicating that the fluctuating wind pressures induced by approaching wind turbulence and vortex shedding is the main cause of the torsional moments.

Fig. 17 compares the spectra of the overall along-wind force, across-wind force and torsional moment with the von Karman spectrum of longitudinal wind velocity.

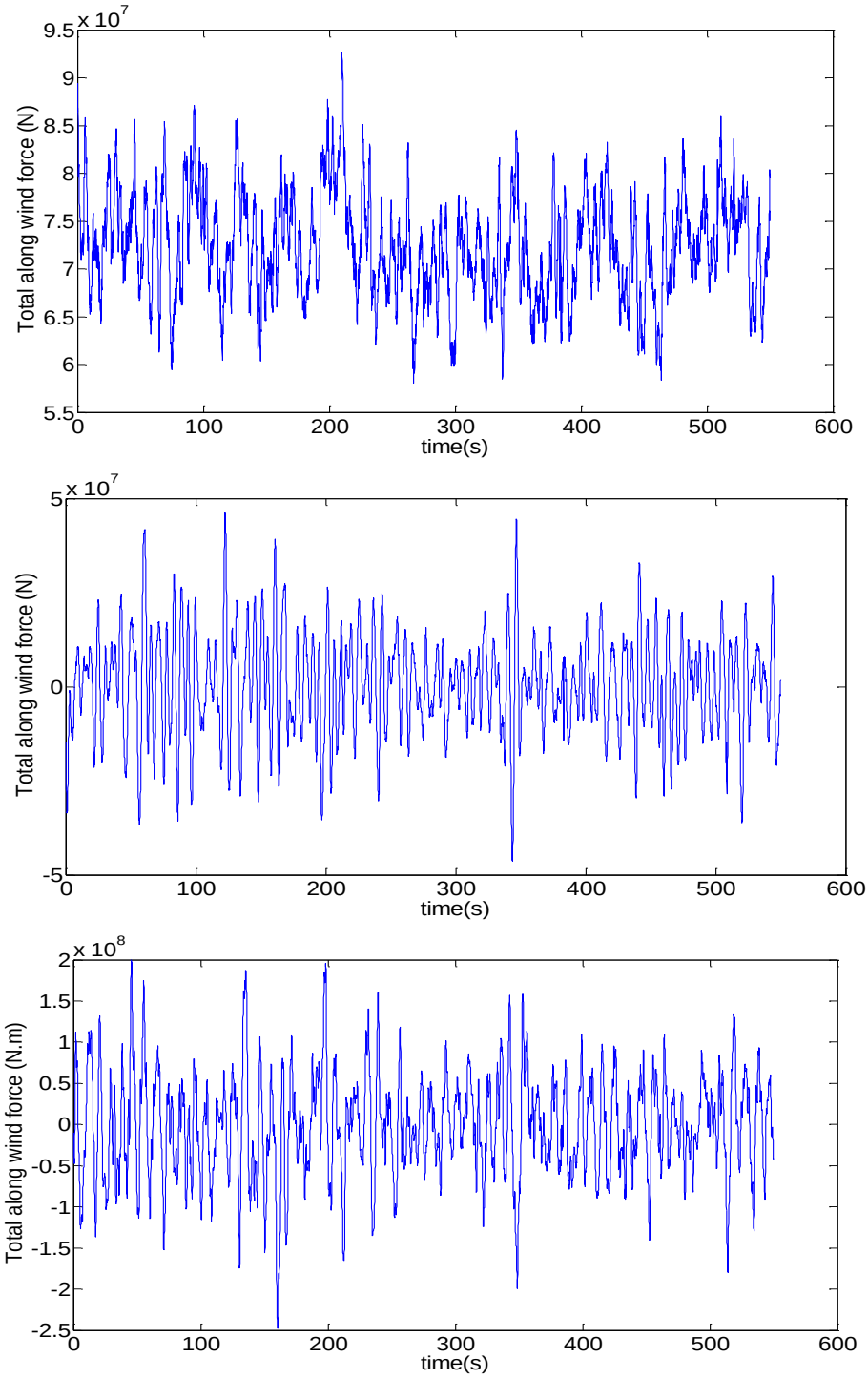

Fig. 11 Time-history of the wind forces F_D, F_L, M

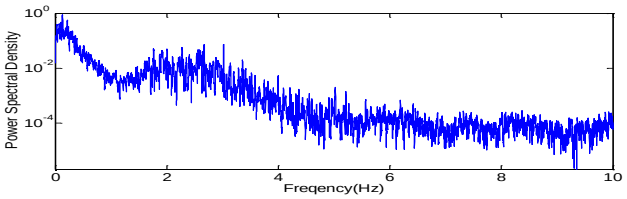

(a) along wind force

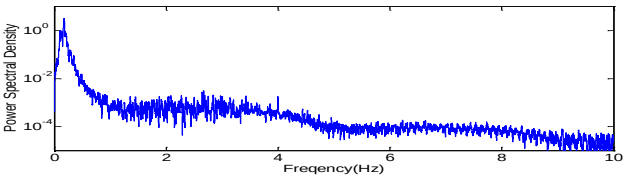

(b) Across wind force

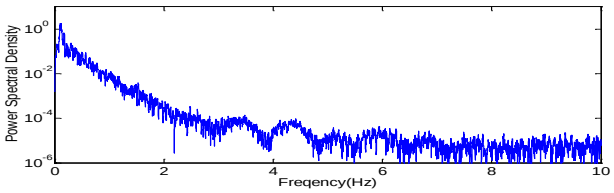

(c) Torsional moment

Fig. 12 Power spectral densities of the overall wind forces

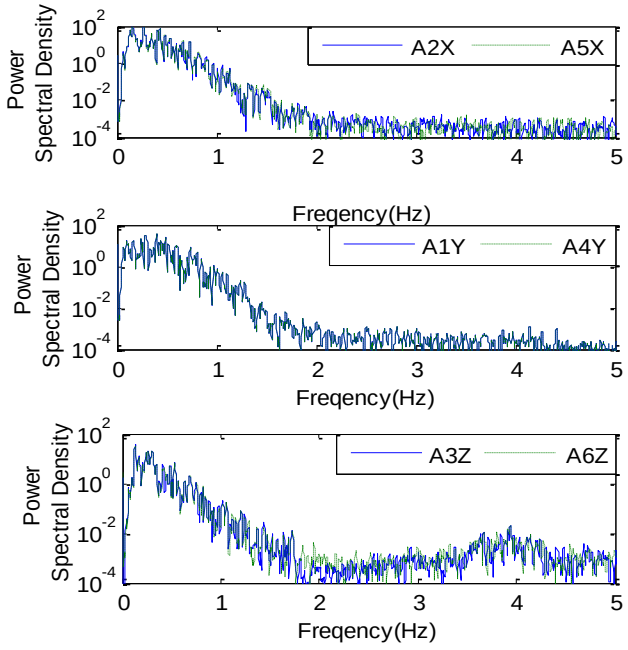

Fig. 13 Power spectral densities of the accelerations at the basement (B5) during Wenchuan earthquake

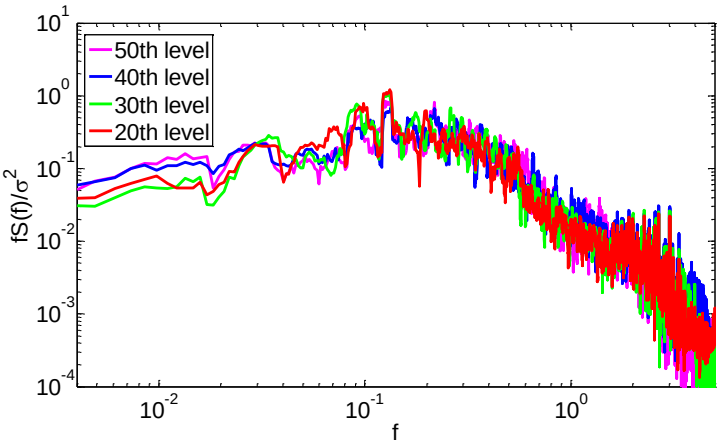

Fig. 14 Along-wind force spectra

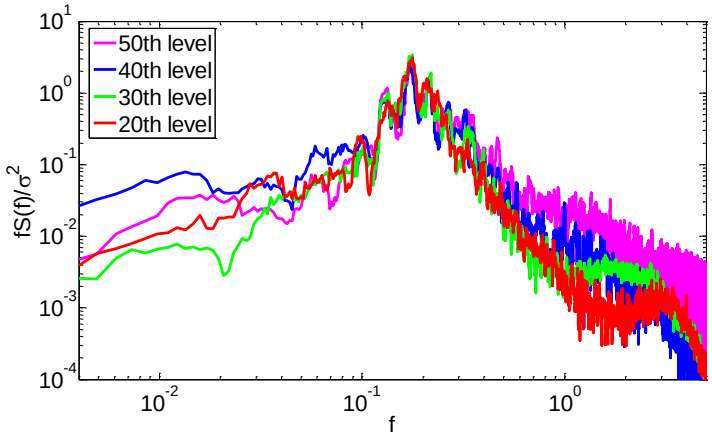

Fig. 15 Across-wind force spectra

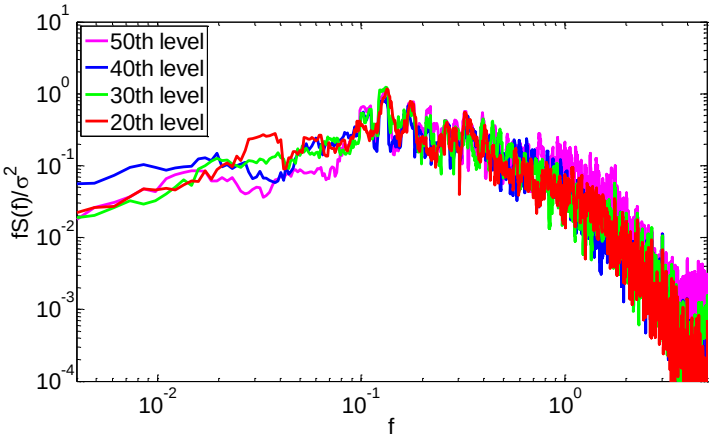

Fig. 16 Torsional moment spectra

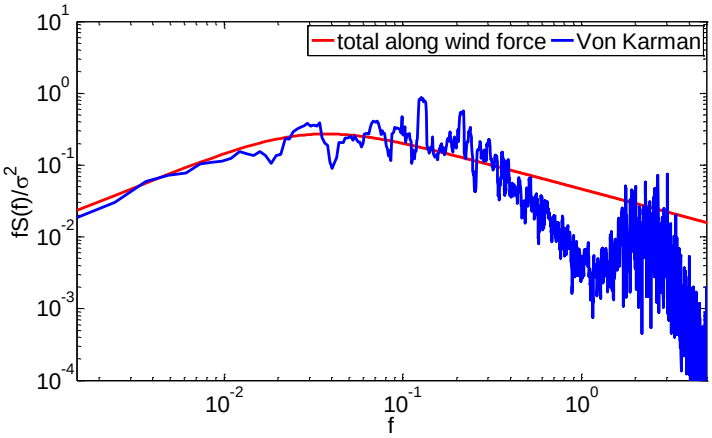

(a) Overall along-wind force spectrum

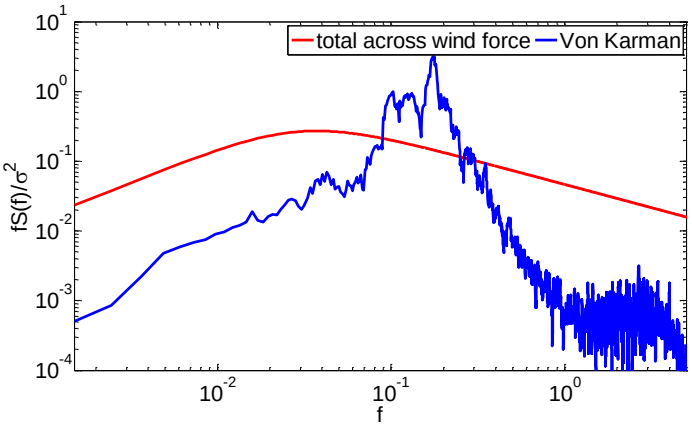

(b) Overall across-wind force spectrum

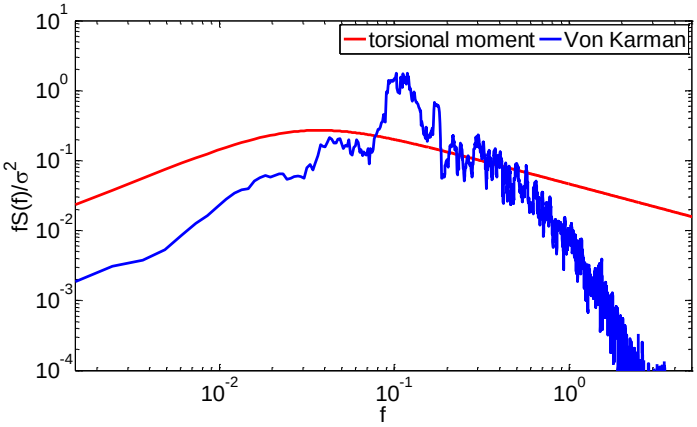

(c) Overall torsional moment spectrum

Fig. 17 Overall wind force spectra

For the along-wind force spectrum, relatively good agreement with the von Karman spectrum is presented. However, in the higher reduced-frequency range, there are some discrepancies between the along-wind force spectrum and the von Karman spectrum. This figure shows the along-wind force spectrum is similar to the approaching wind velocity spectrum generated by the DSRFG method (see Fig. 9), suggesting that the effect of the buffeting due to the oncoming flow is the main cause of the along-wind fluctuating loads on the tall building. That is, the quasi-steady assumption is applicable for predicting the along-wind loads on the tall building.

The distributions of the across-wind force and torsional moment spectra have significant differences from the von Karman spectrum. Hence, the quasi-steady approach is not applicable to the estimations of the across-wind forces and torsional moments.

5.2 Probabilistic characteristics of wind loads

Wind loading is a typical dynamic load, characterized by randomness and uncertainty. To determine the peak values of wind loads for structural design, it is necessary to analyze the probabilistic characteristics of wind loads.

The shape of a probability density function (PDF) can be characterized by its third and fourth central moments (μ_3 and μ_4) relative to the standard deviation value (σ). For a Normal or Gaussian distribution, the skewness coefficient ($S_k = \mu_3/\sigma^3$) and kurtosis coefficient ($K_u = \mu_4/\sigma^4$) are equal to 0 and 3, respectively. The case of $S_k < 0$ corresponds to skewness to the left, while $S_k > 0$ to the right. The case of $K_u > 3$ represents a distribution more peaked at the center than the Gaussian distribution; $K_u < 3$ characterizes distributions flatter at the center than the Gaussian distribution.

The probability density functions of the fluctuating along-wind and across-wind forces as well as torsional moments at layers 50, 40, 30 and 20 are shown in Figs.18-20. Gaussian probability density functions (red curves) are also plotted in these figures for comparison purposes.

Figs. 18-20 show the skewness varies from about zero to a value of 0.2555, and the kurtosis changes in the range between 2.7674 and 3.6484. This is a good indication of the PDF distributions of the wind force components are close to the Gaussian.

5.3 Correlations of the wind loads

The cross-correlation coefficients among the wind forces on different levels of the tall building are calculated and presented in Table 1. For the along-wind forces, the correlation is rather low. The correlation coefficient between the forces on the two highest levels is the largest, but it only has a value of about 0.7. For the across-wind forces, a much higher correlation exists along the building height. The correlation coefficients among adjacent levels have values between 0.7 and 0.9. For the torsional moments, the correlation coefficients between the highest adjacent levels have the largest value of about 0.5. Table 1 shows the wind loads in along-wind direction and torsional motions are poorly correlated while there are higher correlations between the wind forces in the across-wind direction.

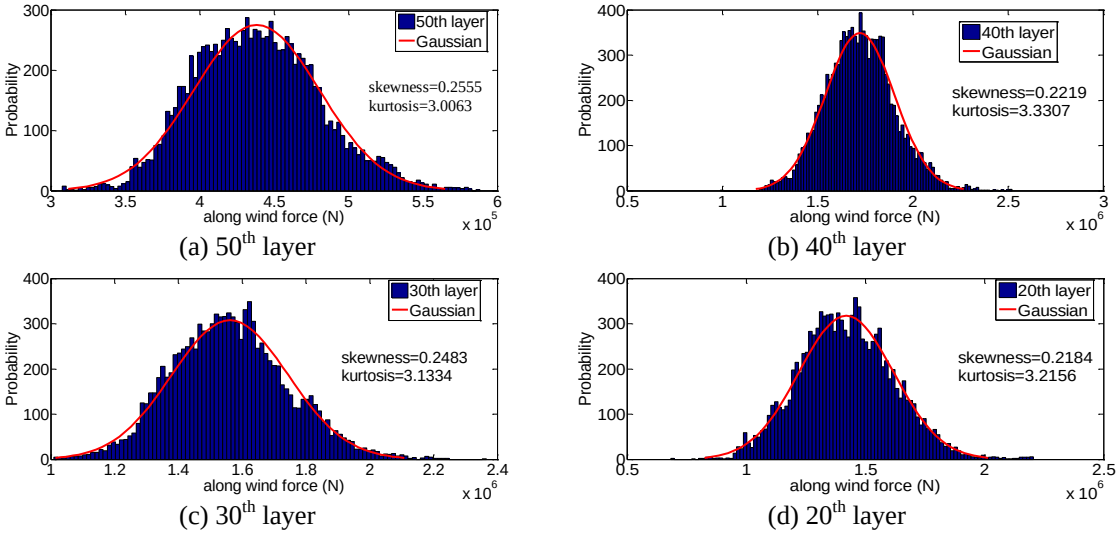

(a) 50th layer (b) 40th layer

(c) 30th layer (d) 20th layer

Fig. 18 Probability density functions of the along-wind forces

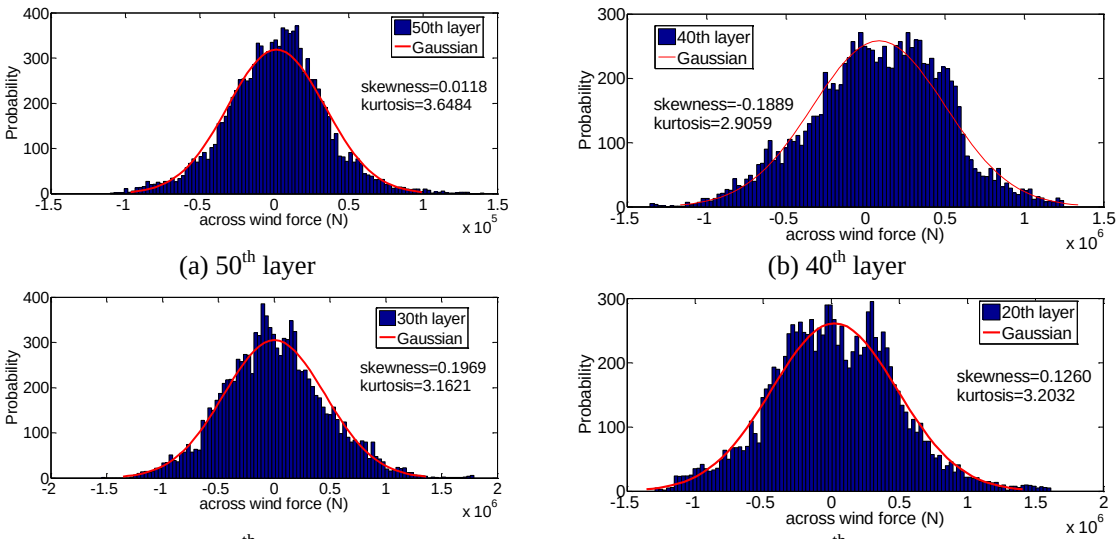

(a) 50th layer (b) 40th layer

(c) 30th layer (d) 20th layer

Fig. 19 Probability density functions of the across-wind forces

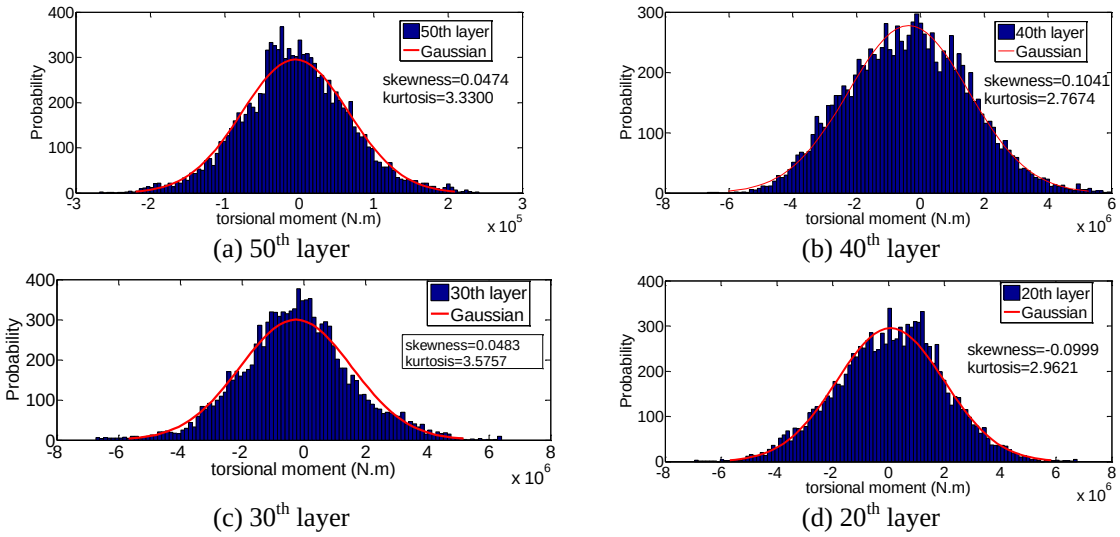

(a) 50th layer (b) 40th layer

(c) 30th layer (d) 20th layer

Fig. 20 Probability density functions of the torsional moments

Table 1 Correlation coefficients between the along-wind forces on different layers

Layer	10	15	20	25	30	35	40	45	50
10	1.00								
15	0.56	1.00							
20	0.35	0.59	1.00						
25	0.21	0.38	0.69	1.00					
30	0.07	0.18	0.37	0.58	1.00				
35	0.06	0.07	0.25	0.39	0.67	1.00			
40	0.09	0.07	0.18	0.24	0.42	0.62	1.00		
45	0.13	0.07	0.13	0.20	0.34	0.52	0.62	1.00	
50	0.08	-0.01	0.05	0.09	0.23	0.41	0.58	0.75	1

6. Wind-induced vibration response analysis

There are two approaches to determine the wind-induced dynamic responses of structures: time-domain method and frequency-domain method. The frequency-domain method is based on the theory of random vibration. At present, the frequency-domain method is widely adopted in estimation of wind-induced vibrations of structures. On the other hand, it is necessary to analyze structural responses in time-domain in some cases, for example, in structural nonlinear response analysis.

To investigate the wind-induced responses of Taipei 101 Tower, the dynamic behavior of the

super-tall building was evaluated for the design wind speed with a 10-year return period. Time-history curves of the wind forces obtained from the LES were directly applied to the three-dimensional finite element (FE) model of the tall building. The wind speed with a 10-year return period at 10 m height above ground is 32 m/s according to the RWDI wind tunnel report of the 101 tower. The damping ratio of Taipei 101 Tower equipped with a big tuned mass damper (TMD) about 660 tone in the building and two smaller TMDs in the pinnacle was assumed to be 5% for the first two vibration modes. The wind-induced responses of the tall building were analyzed in time-domain.

6.1 Three-dimensional FE model

A three-dimensional FE model of the Taipei 101 structural system has been established for the numerical analysis, as shown in Fig. 21. Four kinds of elements are used in establishing the FE model: 3-D beam elements, suitable for nonlinear large rotations and large strains, are utilized to model the columns and beams. Link elements are used to model the brace. Mass elements are used to model the live loads and non-structural components. The floors are modeled with shell elements. The connection between the structure and its foundation is considered to be fixed. The FE model of the super-tall building contains 20532 beam elements, 24048 shell elements, and 3496 link elements.

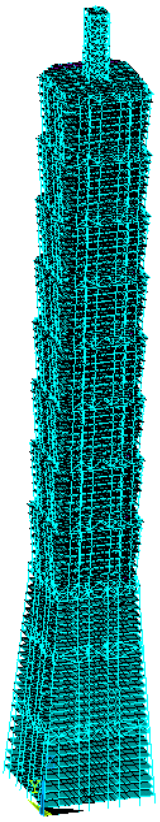

Fig. 21 Finite element model of Taipei 101 Tower

6.2 Natural frequencies

Natural frequency is one of the most important parameters for describing the dynamic characteristics of a tall building. Accurately determining natural frequencies is essential to correctly predicting wind-induced structural responses.

The first three natural frequencies in each translational direction (X and Y) obtained from the field measurements are listed in Tables 4 and 5. These data were obtained from a direct analysis of the acceleration responses measured during three typhoons and the Wenchuan earthquake. The calculated natural frequencies of the first three modes in the X and Y directions and the fundamental natural frequency of torsional movement are compared with the averaged values of the natural frequencies measured during the typhoons and the earthquake, as shown in Table 6. The table shows the differences between the calculated and measured ones are in the range of 5.9%~14%, indicating the FE model is applicable to analyze the wind-induced responses of the tall building.

Table 2 Correlation coefficients between the across-wind forces on different layers

Layer	10	15	20	25	30	35	40	45	50
10	1.00								
15	0.71	1.00							
20	0.34	0.74	1.00						
25	0.13	0.48	0.83	1.00					
30	-0.02	0.24	0.54	0.82	1.00				
35	0.02	0.19	0.38	0.63	0.86	1.00			
40	0.04	0.12	0.24	0.42	0.60	0.78	1.00		
45	0.04	0.09	0.17	0.29	0.43	0.61	0.77	1.00	
50	0.00	0.02	-0.02	-0.07	0.19	0.37	0.57	0.79	1.00

Table 3 Correlation coefficients between the torsional moments on different layers

Layer	10	15	20	25	30	35	40	45	50
10	1.00								
15	0.19	1.00							
20	0.01	0.29	1.00						
25	-0.07	0.09	0.45	1.00					
30	-0.07	0.03	0.21	0.40	1.00				
35	-0.02	0.06	0.12	0.24	0.36	1.00			
40	-0.04	-0.04	0.02	0.13	0.00	0.10	1.00		
45	-0.05	-0.05	0.06	0.15	0.12	0.21	0.06	1.00	
50	-0.05	-0.04	-0.06	-0.03	0.01	0.19	0.11	0.49	1.00

Table 4 Natural frequencies of the first three sway modes

Typhoons or Earthquake Names	Direction X			Direction Y		
	Mode 1 (Hz)	Mode 2 (Hz)	Mode 3 (Hz)	Mode 1 (Hz)	Mode 2 (Hz)	Mode 3 (Hz)
"Masta"	0.156	0.440	0.801	0.147	0.435	0.783
"Talim"	0.156	0.439	0.788	0.147	0.432	0.781
"Krosa"	0.147	0.430	0.772	0.146	0.420	0.762
"Wenchuan"	0.147	0.430	0.781	0.145	0.425	0.772

Table 5 Natural frequencies of the rotational modes

	"Masta"	"Talim"	"Krosa"	"Wenchuan"
Mode 1 (Hz)	0.249	0.244	0.234	0.240
Mode 2 (Hz)	0.596	0.605	0.571	0.586

Table 6 Measured and calculated natural frequencies

Modes	Sway Modes						Rotational Mode
	X Direction			Y Direction			
	Mode 1 (Hz)	Mode 2 (Hz)	Mode 3 (Hz)	Mode 1 (Hz)	Mode 2 (Hz)	Mode 3 (Hz)	Mode 1 (Hz)
Calculated (Hz)	0.161	0.405	0.738	0.161	0.391	0.712	0.276
Measured (Hz)	0.152	0.435	0.786	0.146	0.428	0.775	0.242
Difference (%)*	5.9	6.9	6.1	10.3	8.6	8.1	14.1

*Difference= |(Measured-Calculated)|/Measured

6.3 Mode shape estimation

The first seven mode shapes, which were calculated based on the FE model, including three modes for the translational motion in each horizontal direction (X and Y direction) and one mode for torsional motion about the vertical axis, are shown in Fig. 22.

Figs. 23(a) and 24(a) show the first three sway mode shapes in the X-direction and Y-direction, respectively, determined from the acceleration responses measured during the three typhoons and the Wenchuan earthquake. Meanwhile, the corresponding mode shapes calculated from the FE model are shown in Figs. 23(b) and 24(b) for comparison purposes. The mode shapes presented in

this paper have been conventionally normalized toϕ=1 at the 101st floor for each mode. These figures show that the mode shapes determined from the FEM analysis are generally consistent with the field measurement results.

6.4 Wind-induced responses

The use of high strength materials and advanced design methods has resulted in flexible and low damped super-tall buildings. Such buildings may experience excessive deflections and accelerations under strong winds. Wind-excited vibration may damage curtain walls or cause discomforts of occupants. For super-tall buildings, such as Taipei 101 Tower, keeping the wind-induced motions during strong wind storms within acceptable limits may be a more challenge task than ensuring that they have sufficient structural strength. It has been widely accepted that building acceleration is the most common index for evaluating structural serviceability performance under wind actions.

The time-histories of displacements and accelerations in along–wind (X-direction) and across-wind (Y-direction) at the center on the top occupied floor (89th floor) are shown in Figs. 25 and 26.

The correlation coefficients among the displacement responses in the X and Y directions on different floors were calculated and are presented in Table 7. It is observed that the correlation coefficients between the along-wind displacements or the across-wind displacements on different floors are high, while those between the along-wind displacements and the across-wind displacement are very low. This implies that the vibration modes in the two horizontal principal axes do not couple with each other. Therefore, the wind-induced responses of the three-dimensional structure can be calculated and analyzed separately.

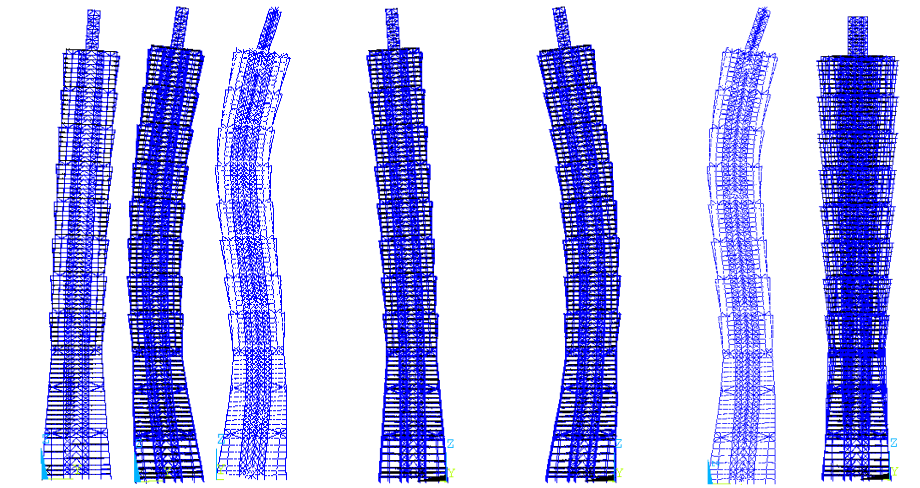

Fig. 22 Calculated mode shapes of Taipei 101 Tower

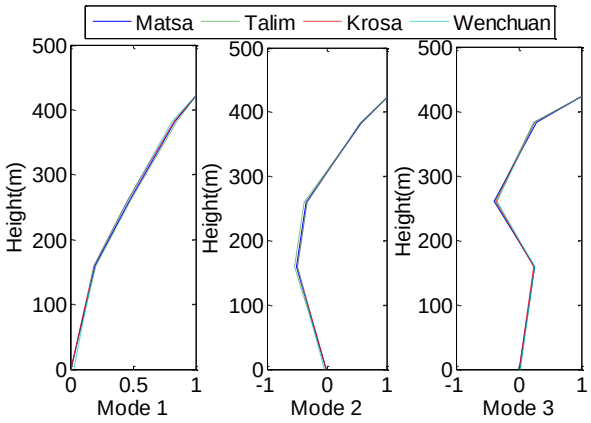

(a) Measured mode shapes during the three typhoons and Wenchuan earthquake

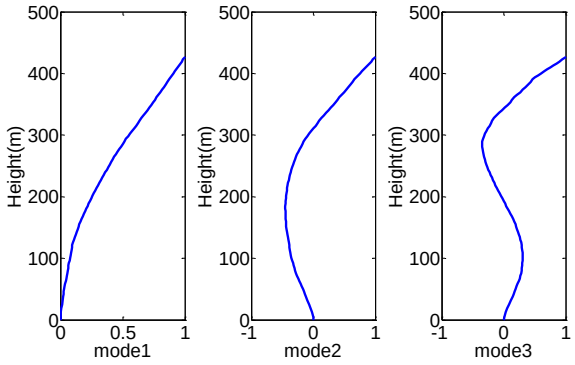

(b) Calculated

Fig. 23 Measured and calculated mode shapes in X direction of the Taipei 101 Tower

Table 7 Correlation coefficients between the across-wind forces on different floors

	ux20	ux40	ux60	ux80	ux100	uy20	uy40	uy60	uy80	uy100
ux20	1.000									
ux40	0.973	1.000								
ux60	0.903	0.975	1.000							
ux80	0.845	0.938	0.991	1.000						
ux100	0.805	0.908	0.977	0.996	1.000					
uy20	0.120	0.128	0.128	0.125	0.124	1.000				
uy40	0.130	0.142	0.143	0.142	0.141	0.991	1.000			
uy60	0.137	0.151	0.155	0.154	0.154	0.971	0.994	1.000		
uy80	-.140	-.156	-.160	0.159	0.159	0.9561	0.985	0.998	1.000	
uy100	-.141	0.157	0.162	-.162	-.161	0.9461	0.978	0.995	0.999	1.000

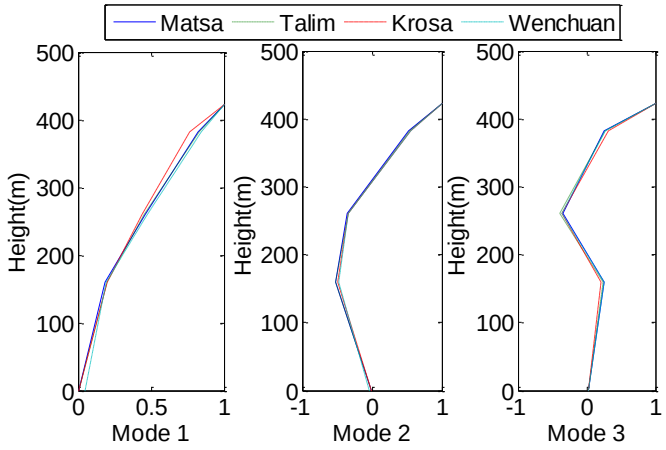

(a) Measured mode shapes during three typhoons and Wenchuan earthquake

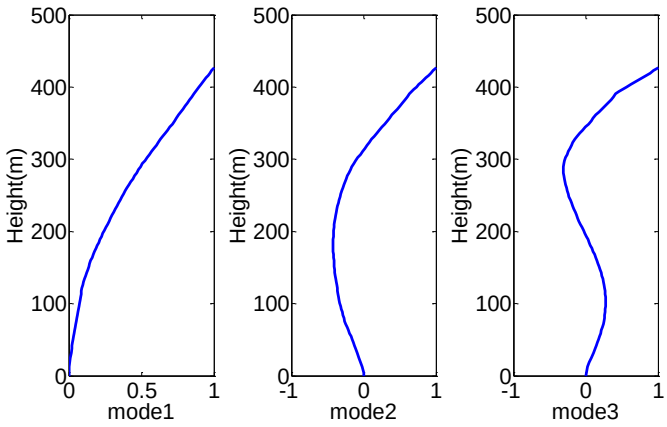

(b) Calculated

Fig. 24 Measured and calculated mode shapes in Y direction of the Taipei 101 Tower

The largest dynamic displacement and acceleration of the building at height z can be expressed as

$$d_{\max}^{k}(z) = g\sigma_k(z) \qquad k=x, y \tag{10}$$

$$a_{\max}^{k}(z) = g\sigma_k(z) \qquad k=x, y \tag{11}$$

where g is peak factor and $\sigma_k(z)$ is the rms value of the wind displacement or acceleration components. To determine a suitable peak factor, the PDFs of the fluctuating along-wind and across-wind displacements at floors 100, 80, 60 and 40 are plotted in Figs. 26 and 27, in which the skewness and the kurtosis are listed. These figures show the PDFs of the two response components are Gaussian distributions. Hence, in this paper, the peak factor takes 3.5.

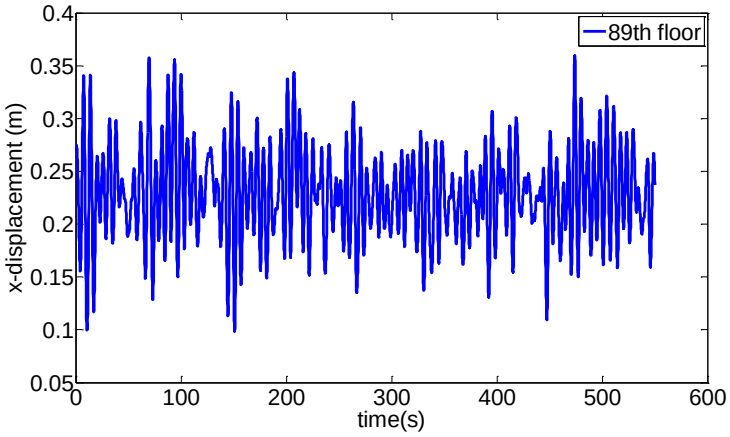

(a) Along-wind displacement

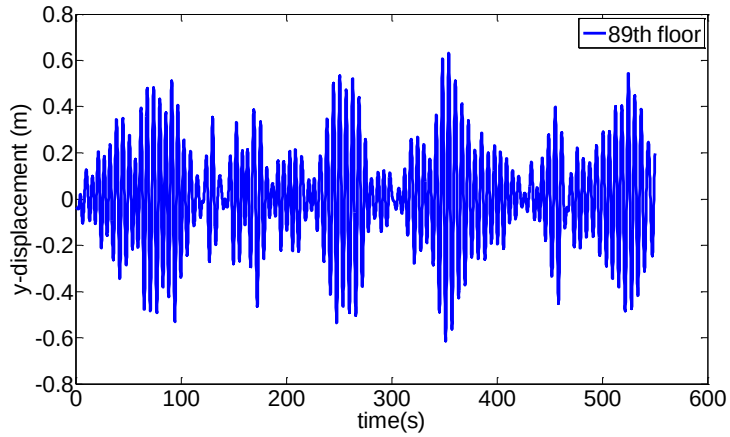

(b) Across-wind displacement

Fig. 25 Time-history of wind-induced displacements at the center of the top occupied floor

The maximum displacement of the structure in the X or Y direction under the wind actions can be expressed as

$$D_{\max}^{k}(z) = d_{s}^{k}(z) + d_{\max}^{k}(z) \tag{12}$$

where, $d_{s}^{k}(z)$ is the mean displacement and $d_{\max}^{k}(z)$ is the maximum dynamic displacement at the building height of *z*. Neglecting the cross terms, the total peak acceleration response at the center on a floor at the height of z can be expressed as follows (International Standards Organization Wind Load Committee 1987)

$$a_{\max}(z) = 0.8[(\sigma_{\max}^{x}(z))^{2} + (\sigma_{\max}^{y}(z))^{2}]^{0.5} \tag{13}$$

The displacements and accelerations at the central locations of the building floors in the X and Y directions were determined, as shown in Figs. 28 and 29. The wind-induce response curves take

the shape of a deforming cantilever and are relatively smooth without obvious inflexions. The maximum and rms responses of displacement and acceleration in across-wind direction are larger than those in along-wind direction. This suggests that the across-wind response dominates the dynamic response of Taipei 101 Tower. Therefore, the across-wind responses and forces should be considered in the wind-resistant design of super-tall buildings. However, most current codes and standards provide limited information or guidelines to determine the across-wind responses and forces for tall buildings. In such cases, wind tunnel tests or CFD simulations (e.g., LES) are required for the wind-resistant design of such structures.

Table 8 summarizes the calculated maximum acceleration responses at the center on the top occupied floor (the 89th floor, at height of 382.2 m from ground), while the wind tunnel test results (RWDI 1999) are also presented for comparison purposes. It can be seen from the table that the predicted results are consistent with the model test data. The discrepancies between the calculated and wind tunnel test results are less than 13%, which are accepted in engineering practices.

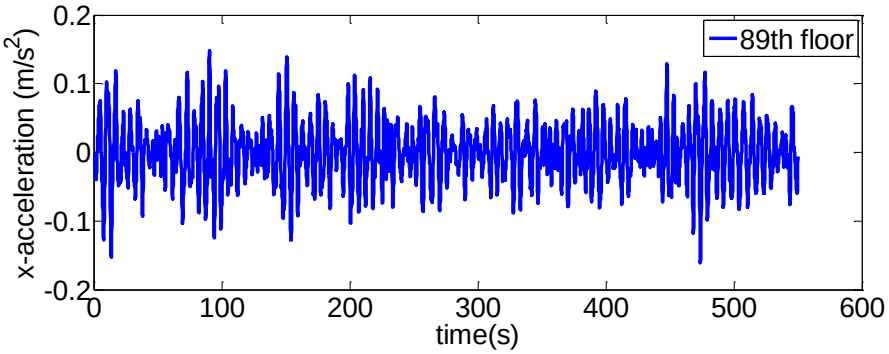

(a) Along-wind acceleration

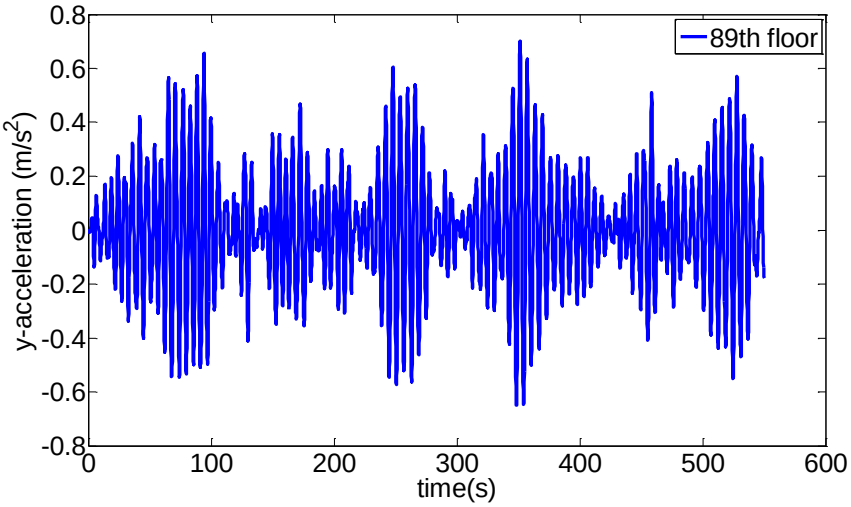

(b) Across-wind acceleration

Fig. 26 Time-history of wind-induced acceleration at the center of the top occupied floor

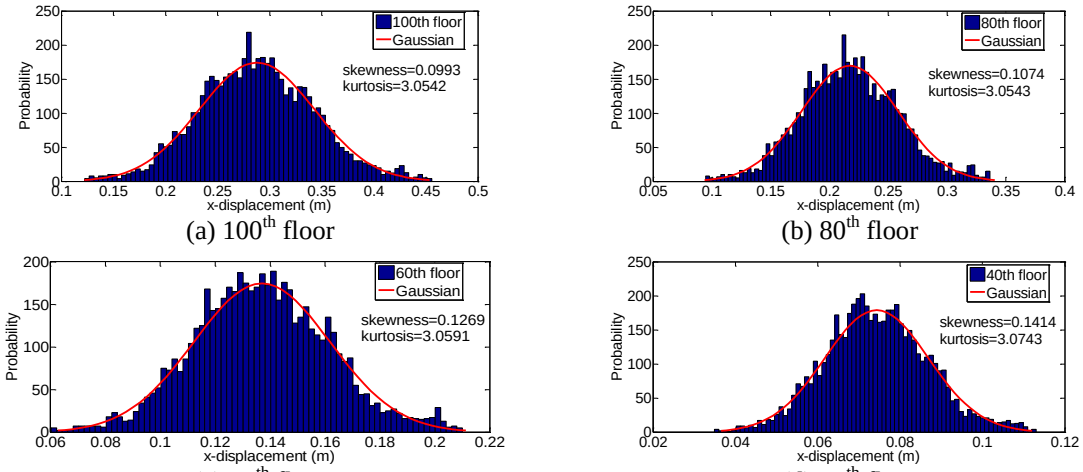

(a) 100th floor (b) 80th floor

(c) 60th floor (d) 40th floor

Fig. 27 Probability density functions of the torsional moments

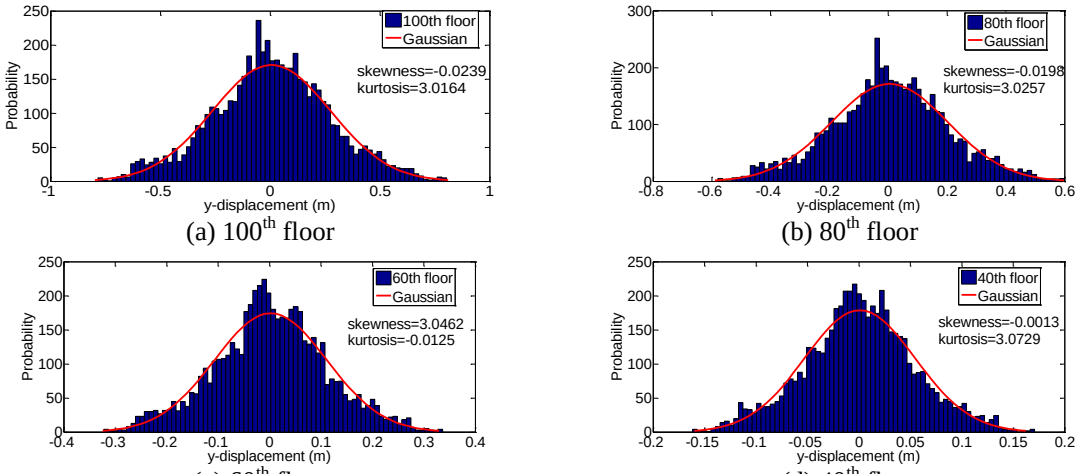

(a) 100th floor (b) 80th floor

(c) 60th floor (d) 40th floor

Fig. 28 Probability density functions of the across-wind displacements

Table 8 The maximum overall accelerations at the center on the top occupied floor

	Damping Ratio		Returned Period (Years)
	1.5%	5%	
Calculated (m/s^2)	1.13	0.65	10
Wind tunnel test (m/s^2)	1.003	0.58	
Difference (%)*	12.6	12	

6.5 Power spectral analysis of the wind-induced responses

To investigate the wind-induced vibration characteristic of the super-tall building, spectral analysis of the displacement and acceleration responses at different floors were conducted. The normalized power spectral densities of the calculated displacement and acceleration responses in the X direction and Y direction are shown in Figs. 29 and 30, respectively. An obvious peak occurs at 0.17 Hz either in Fig. 29 or in Fig. 30. Such a peak actually corresponds to the first translational natural frequency in the X direction or Y direction. While the power spectra curves of the accelerations display the second peak at frequencies of 0.39Hz in along-wind direction and 0.41 Hz in across-wind direction, matching the second translational natural frequencies in the two directions. These figures indicate that the first mode dominates the responses of displacement and acceleration in the X-direction or Y direction, while the second mode has some effects on the acceleration responses. The magnitudes of the PSD of the displacement and acceleration at the frequencies corresponding to the spectral peaks in both directions increase with the building elevation.

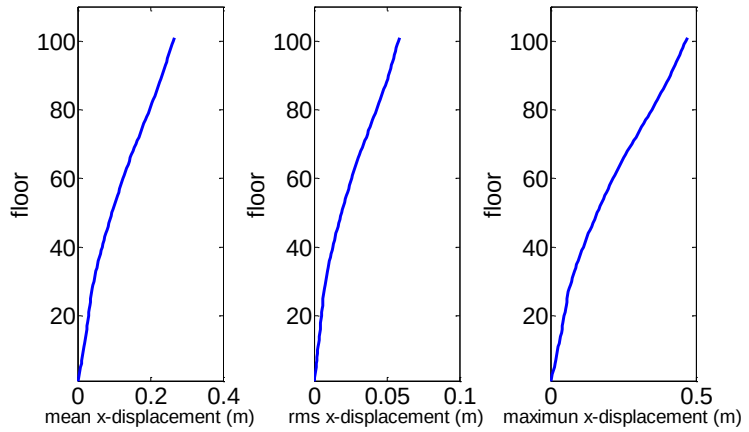

(a) Along-wind displacement

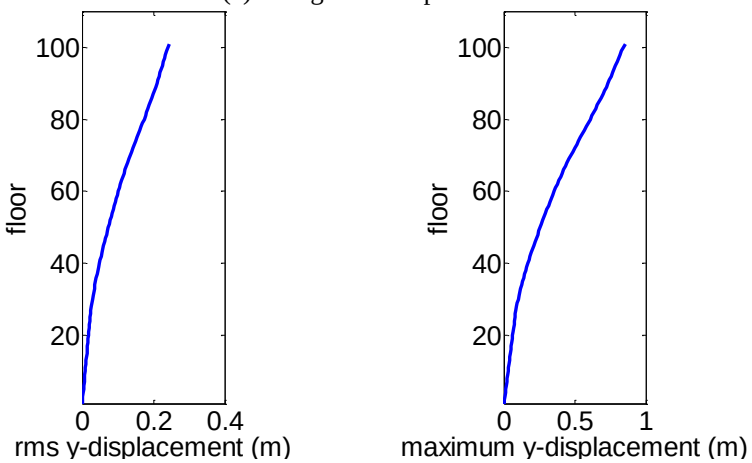

(b) Across-wind displacement

Fig. 29 Displacement distributions along the building elevation

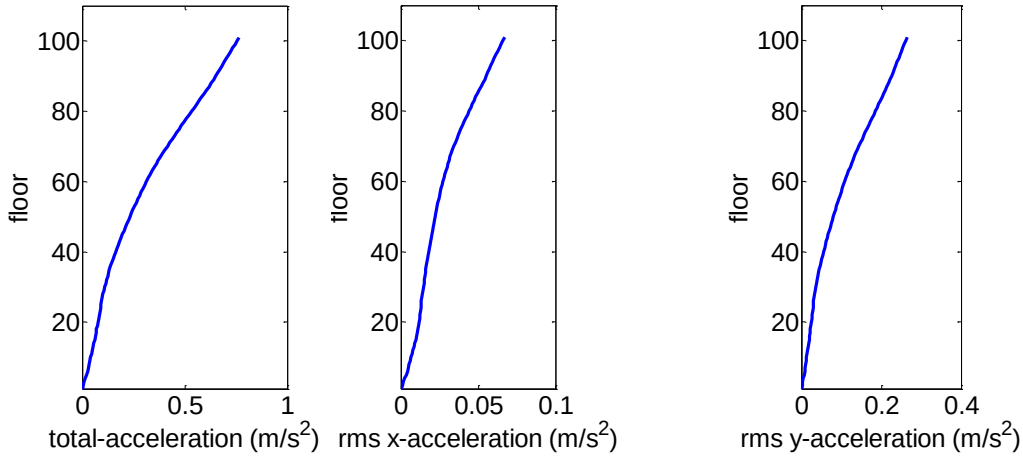

Fig. 30 Wind-induced acceleration distribution along the building elevation

The normalized power spectral densities of the calculated accelerations at the top occupied floor in the two directions and those obtained from the field measurements are shown in Fig. 31 for comparison purposes. These figures show the spectra of the calculated accelerations in along-wind direction and across-wind direction basically agree well with those from the field measurements. The calculated spectra are lower in magnitude in the low and high frequency ranges than those obtained from the measurements. There are some reasons to cause the discrepancies, for example, the incident wind direction in the field measurements may differ from that in the numerical simulation, and absence of surrounding buildings around Taipei101 Tower in the present computations resulted in discrepancies.

7. Equivalent static wind loads

The equation of motion of a Multi-Degrees of Freedom system subjected to random wind loads is expressed as follows

$$[\mathrm{M}]\{\ddot{\mathrm{y}}\}+[\mathrm{C}]\{\dot{\mathrm{y}}\}+[\mathrm{K}]\{\mathrm{y}\}=\{\mathrm{P(t)}\} \tag{14}$$

where [M],[C] and [K] are the mass matrix, damping matrix and stiffness matrix of the structure, respectively. $\{y\}$ is the displacement vector. $\{P(t)\}$ is the vector of wind excitation, in this study, which is obtained by the LES. Based on this equation, the wind-induced dynamic responses of the tall building under wind actions can be determined through the time-domain or frequency-domain analysis.

In the time-domain analysis, the computational algorithm is based on an incremental load-displacement equation. After the structural dynamic responses are obtained, the equivalent static wind loads (ESWLs) on the tall building can be determined by the equations below.

$$\hat{F}(y_i)=\bar{F}(y_i)\pm gM(y_i)\sigma_a(y_i) \tag{15}$$

where $\hat{F}(y_i)$ is the equivalent static wind load at the i-th floor of the building in the time-domain; $\bar{F}(y_i)$ is the mean wind load at the i-th floor; g is the peak factor; $gM(y_i)\sigma_a(y_i)$ is the inertial wind force at the i-th floor. $M(y_i)$ is the mass of the i-th floor; $\sigma_a(y_i)$ is the rms acceleration at the i-th floor determined from the structural dynamic analysis.

In the frequency domain, the structural displacement vector $\{y\}$ is decomposed into

$$\{y\} = [\phi]\{q\} = \sum_{j=1}^{m} \phi_j q_j \tag{16}$$

where $[\phi]$ is the $N \times m$ mode shape matrix corresponding to the lowest m vibration modes; N is the total nodes number of the structure. $\{q\}$ is the vector of the generalized displacement and q_j is the j-th component of vector $\{q\}$.

By assuming the damping matrix [C] to be proportional to [M] and [K], substituting Eq. (16) into Eq. (14) and pre-multiplying each term in the ensuing equation by transposing of the corresponding mode shape $\{\phi\}_j^T$, Eq. (14) can be reduced into

$$\ddot{q}_j + 2\xi_j\omega_j \dot{q}_j + \omega_j^2 q_j = \frac{P_j^*(t)}{M_j^*} \tag{17}$$

$$M_j^* = \{\phi\}_j^T [M]\{\phi\}_j \tag{18}$$

$$P_j^* = \{\phi\}_j^T P(t) \tag{19}$$

where ω_j and ξ_j are the natural frequency and damping ratio respectively for the j-th mode; M_j^* and P_j^* are the generalized mass and force.

Based on the random vibration theory, the power spectral density (PSD) of the displacement response at the location of the i-th floor of the building would be

$$S_r(y_i, \omega) = \sum_{j=1}^{m}\sum_{k=1}^{m} \phi_{ij}\phi_{ik} H_j^*(\omega) H_k(\omega) S_{f_j f_k}(\omega) \tag{20}$$

where $S_{f_j f_k}(\omega) = \dfrac{S_{P_j^* P_k^*}(\omega)}{M_j^* M_k^*} = \dfrac{\{\phi\}^T [S_{P_l P_m}(\omega)]\{\phi_k\}}{M_j^* M_k^*} = \dfrac{1}{M_j^* M_k^*} \sum_{l=1}^{N}\sum_{m=1}^{N} S_{P_l P_m}(\omega)\phi_{jl}\phi_{km}$

$S_{P_l P_m}$ is the cross-PSD function of the fluctuating along-wind or across-wind loads.

The frequency response function $H_j(\omega)$ of the j-th vibration mode is

$$H_j(\omega) = \frac{1}{(\omega_j^2 - \omega^2 + 2i\xi_j\omega\omega_j)} \quad , \quad i = \sqrt{-1} \tag{21}$$

For a tall building structure, the cross-correlation terms in Eq. (20) are usually neglected, giving the following approximate expression.

$$S_r(y_i,\omega)=\sum_{j=1}^{m}\phi_j^2\,|H_j(\omega)|^2\,S_{f_j}(\omega) \tag{22}$$

where $S_{f_j}(\omega)$ is the auto-PSD function of the local wind load for the j-th mode.

The PSD of the displacement response for the j-th mode at the i-th floor can be expressed as

$$S_{rj}(y_i,\omega)=\phi_j^2\,|H_j(\omega)|^2\,S_{f_j}(\omega) \tag{23}$$

The standard deviation of the displacement for the j-the mode at the i-th floor is determined by integrating its PSD as follows

$$\sigma_{rj}(y_i)=\sqrt{\int_0^\infty S_{rj}(y_i,\omega)d\omega} \tag{24}$$

The standard deviation of the inertial wind load at the i-th floor is

$$\sigma_P(y_i)=m(y_i)\sum_{j=1}^{m}\omega_j^2\sigma_{rj} \tag{25}$$

where $m(y_i)$ is the mass of the i-th floor.

The equivalent static wind load on the structure would be

$$\hat{P}(y_i)=\bar{P}(y_i)\pm g\sigma_P(y_i) \tag{26}$$

where $\hat{P}(y_i)$ is the equivalent static wind load at the i-th floor of the building; $\bar{P}(y_i)$ is the mean wind load at the i-th floor; g is the peak factor; $g\sigma_P(y_i)$ is the peak inertial wind force at the i-th floor.

In this study, the first three modes (the mode shapes are shown in Figs. 23 and 24) were considered to calculate the ESWLs on Taipei 101 Tower in the frequency-domain.

7.1 Comparison with wind tunnel test results

The wind-induced overturning moments and shear forces at the base of the tall building, which were calculated in the time-domain and frequency-domain, are listed in Table 9 and are compared with the wind tunnel test results obtained by RWDI (RWDI 1999).

The wind tunnel test (RWDI 1999), which employed the High Frequency Force Balance technique, considered the fundamental mode shapes for swaying and twisting motions to determine the equivalent static wind loads on Taipei 101 Tower. The fundamental natural frequencies of 0.1586 Hz for the X direction, 0.1587 Hz for the Y direction in swaying motions and 0.2170 Hz for torsional motion were adopted in the wind tunnel test (RWDI 1999).

Table 9 shows the ESWL' results calculated by the time-domain and frequency-domain methods are consistent. Besides, the calculated shear force in the X direction (along-wind direction) and overturning moment around the X-axis agree well with the wind tunnel test results. However,

the calculated shear force in the Y direction (across-wind direction) and overturning moment around the Y-axis are larger than the model test results. These discrepancies may be caused by several reasons, including: (1) there are differences of the natural frequencies and profiles of turbulence parameters adopted in the wind tunnel test and in the computation; (2) Isolated Taipei 101 Tower was considered in the LES while the major surrounding buildings around the tall building were included in the wind tunnel test.

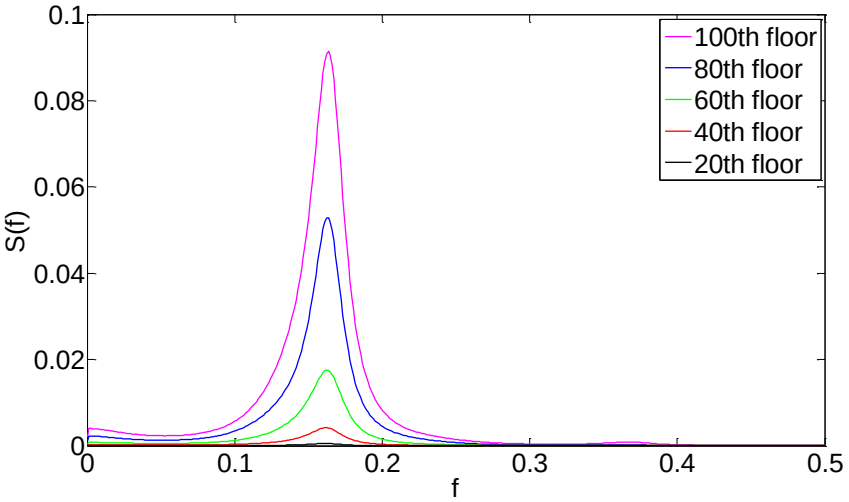

(a) Along-wind displacement

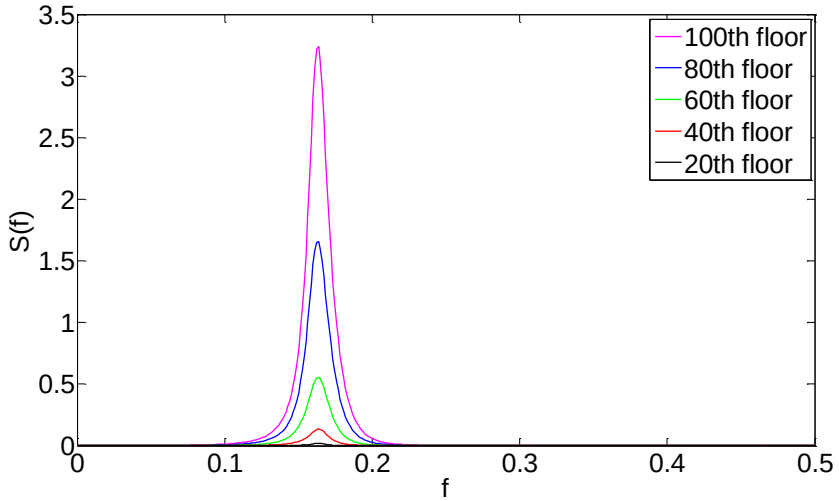

(b) Across-wind displacement

Fig. 31 Power spectra of the wind-induced displacement at different floors

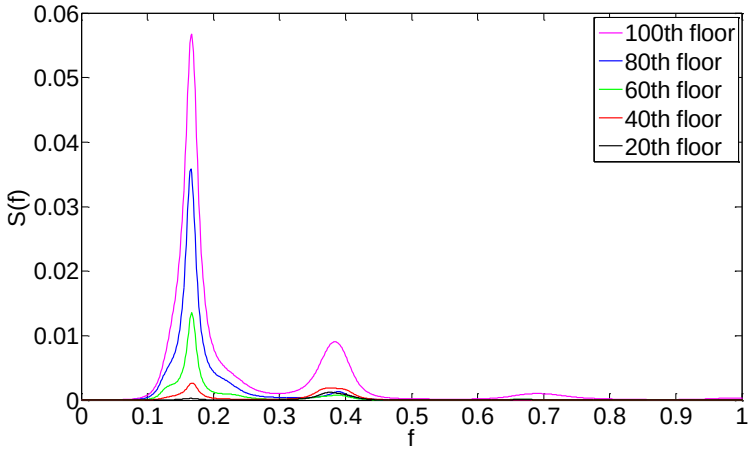

(a) Along-wind displacement

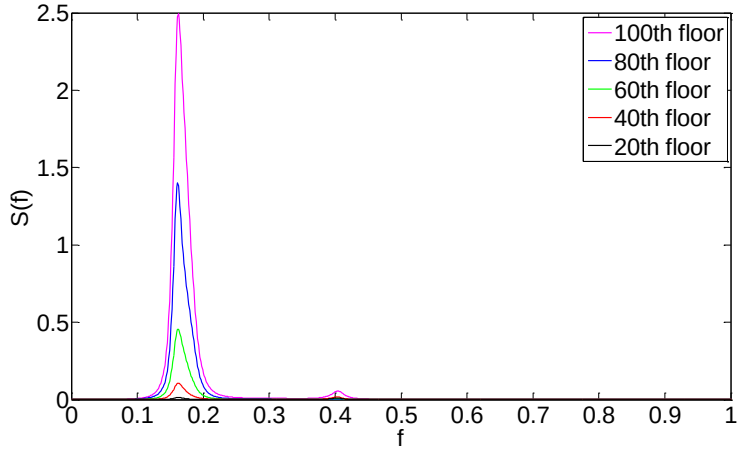

(b) Across-wind displacement

Fig. 32 Power spectra of the wind-induced displacement at different floors

Table 9 Structural design wind loads

	Mx (10^{10}N-m)	My (10^{10}N-m)	Fx (10^{8}N)	Fy (10^{8}N)
Wind tunnel test	2.813	2.797	1.148	1.123
Calculated in time domain	2.488	4.484	1.126	1.621
Calculated in frequency domain	2.750	4.791	1.1	1.581

Structural Damping Ratio: $\zeta = 2.0\%$

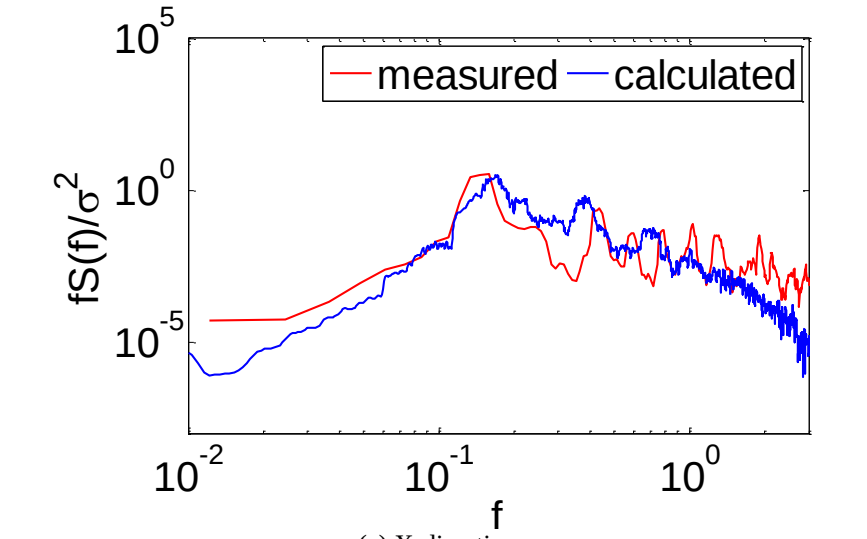

(a) X-direction

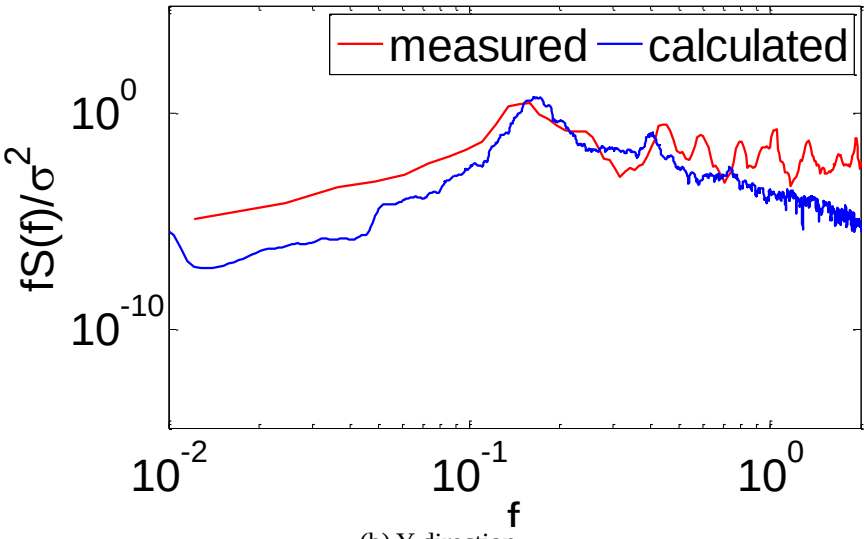

(b) Y-direction

Fig. 33 Power spectra of the measured and calculated accelerations at the top occupied floor

8. Conclusions

Based on the wind loads on Taipei 101 Tower obtained by the new inflow turbulence generator (DSRFG) and new SGS model, the wind-induced dynamic responses of the super-tall building were calculated using the 3D FE model of the high-rise structure. Furthermore, the equivalent static wind loads on the building were determined by the time-domain and frequency-domain methods. The predicted results were compared with the field measurements and wind tunnel test results to verify the accuracy and reliability of the newly proposed numerical models and methods.

The major conclusions from the combined numerical and experimental study are summarized below:

(1) The inflow turbulence generator (DSRFG) was proved to be able to produce a spatially correlated turbulent flow field satisfying any target spectrum such the von Karman spectrum and prescribed profiles of turbulence intensity and turbulence integral length scale.

(2) Unlike the majority of the past studies on LES of wind effects on tall buildings, the present LES was conducted for the full-scale sizes of Taipei 101 Tower with Reynolds number of 1.8×10^8 based on the approaching wind speed at 10m height and base width of the building. The computed wind-induced responses and the equivalent static wind loads were in satisfactory agreement with the field measurements and wind tunnel test results. This illustrated that the new SGS model is suitable for relative coarse grid situations and high Reynolds number flows.

(3) The wind-induced dynamic responses and the ESWLs of Taipei101 Tower in across-wind direction were much larger than those in along-wind direction. Therefore, the across-wind responses and forces must be considered in the wind-resistant design of super-tall buildings.

In summary, the LES integrated with the DSRFG technique and the new SGS model could provide satisfactory predictions of the wind effects on the super-tall building. It is encouraging to obtain the numerical results comparable with the field measurements and the wind-tunnel test estimations. The numerical frameworks presented in this paper, including the recommended SGS model, the inflow turbulence generation technique and the associated numerical treatments, are expected to be useful in practice for evaluation of the design wind loads on tall buildings.

Acknowledgements

The work described in this paper was fully supported by grants from the National Natural Science Foundation of China (Project No: 51178179, 91215302 and 51378484).

References

Baker, CJ. (2007), "Wind engineering—past, present and future", *J. Wind Eng. Ind. Aerod.*, **95**(9-11), 843-870.

Cheung, J.C.K. and Holmes, J.D., Melbourne, W.H., Lakshmanan, N. and Bowditch, P. (1997), "Pressures on a 1/10 scale model of the Texas Tech Building", *J. Wind Eng. Ind. Aerod*., **69-71**, 529-538.

Cochran, L.S. and Cermak, J.E. (1992), "Full- and model-scale cladding pressures on the Texas Tech University experimental buildings", *J. Wind Eng. Ind. Aerod*., **43**(1-3), 1589-1600.

Huang, S.H. and Li, Q.S. (2010), "A new dynamic one-equation subgrid-scale model for large eddy simulations", *Int. J. Numer. Meth. Eng*., **81**(7), 835-865.

Huang, S.H., Li, Q.S. and Xu, S. (2007), "Numerical evaluation of wind effects on a tall steel building by CFD", *J. Constr. Steel Res*., **63**(5), 612-627.

Huang, S.H., Li. Q.S. and Wu, J.R. (2010), "A general inflow turbulence generator for large eddy simulation", *J. Wind Eng. Ind. Aerod*., **98**(10-11), 600-617.

International Standards Organization Wind Load Committee (1987), Proposal for wind loading standard, ISO TC 98/SC3/WG2, 1987.

Jeary, AP. (1986), "Damping in tall buildings, a mechanism and a predictor", *Earthq. Eng. Struct. D*., **14**(5), 773-750.

Kajishima, T. and Nomachi, T. (2006), "One-equation subgrid scale model using dynamic procedure for the

energy production", *J. Appl. Mech. T. – ASME*, **73**(3), 368-373.
Kim, W.W. and Menon, S. (1997), Application of the localized dynamic subgrid-scale model to turbulent with wall-bounded flows, *Technical report AIAA-97-0210. Reno(NV): American Institute of Aeronautics and Astronautics, 35th Aerospance Sciences Meeting*.
Li Q.S., Zhi, L.H. and Hu, F. (2010), "Boundary layer wind structure from observation on a 325 m tower", *J. Wind Eng. Ind. Aerod.*, **98**(12), 818-832.
Li, Q.S., Xiao, Y.Q. and Wong, C.K. (2005), "Full-scale monitoring of typhoon effects on super tall buildings", *J. Fluid. Struct*., **20**(5), 697-717.
Li, Q.S., Xiao, Y.Q., Wu, J.R., Fu, J.Y. and Li, Z.N. (2008), "Typhoon effects on super-tall buildings", *J. Sound Vib*., **313**(3-5), 581-602.
Li, Q.S., Zhi, L.H. and Hu, F. (2009), "Field monitoring of boundary layer wind characteristics in urban area", *Wind Struct*., **12**(6), 553-574.
Li,Q.S and Melbourne, W.H. (1996), "Pressure fluctuations on The Texas Tech Building model in various turbulent flows", *Proceedings of Bluff Body Aerodynamics and Application*, Blacksburg, AIX9-AIX12.
Littler, J.D. and Ellis, B.R. (1992), "Full scale measurements to determine the response of Hume Point to wind loading", *J. Wind Eng. Ind. Aerod*., **42**(1-3), 1085-1096.
Murakami, S. (1998), "Overview of turbulence models applied in CWE-1997", *J. Wind Eng. Ind. Aerod*., **74-76**, 1-24.
Nicoud, F. and Ducros, F. (1999), "Subgrid-scale stress modeling based on the square of the velocity gradient tensor flow", *Turbul. Combustion*, **62**(3), 183-200.
Nozawa, K. and Tamura, T. (2002), "Large eddy simulation of the flow around a low-rise building immersed in a rough-wall turbulent boundary layer", *J. Wind Eng. Ind. Aerod*., **90**(10), 1151-1162.
Nozawa, K. and Tamura, T. (2005), "Large eddy simulation of wind flows over large roughness elements", *In:Proceedings of EACWE4* 2005.
Ohkuma, T., Marukawa, H., Niihori, Y. and Kato, N. (1991), "Full-scale measurement of wind pressures and response accelerations of a high-rise building", *J. Wind Eng. Ind. Aerod*., **38**(2-3), 185-186.
Okada, H. and Ha, Y.C. (1992), "Comparison of wind tunnel and full-scale pressure measurement tests on the Texas Tech building", *J. Wind Eng. Ind. Aerod*., **43**(1-3), 1601-1612.
Research Institute of Building & Construction (1999), Report on the structural design scheme of Taipei 101. Evengreen Consulting Engineering, Inc, Taipei.
Rowan Williams Davies and Irwin Inc. (1999), "Wind-induced structural responses cladding wind loads study".
Shiau, B.S. (2000), "Velocity spectra and turbulence statistics at the northeastern coast of Taiwan under high-wind conditions", *J. Wind Eng. Ind. Aerod*., **88**(2-3), 139-151.
Stathopoulos, T. (19997), "Computational wind engineering: past achievements and future challenges", *J. Wind Eng. Ind. Aerod*., **67-68**, 509-532.
Tracy, K.C. and Pirnia, J.D. (2007), "Dynamic behavior of tall buildings under wind: insights from full-scale monitoring", *Struct. Des. Tall Spec. Build*., **16**, 471-486.
Tracy, K.C., Pirnia, J.D., Bashor, P.R., Kareem, A., Kilpatrick, J., Young, B., Galsworthy, J., Isyumov, N., Morrish, D. and Bake, W. (2007), "Full-scale performance evaluation of tall buildings under winds", *Proceedings of the 12th International Conference on Wind Engineering, Cairns.*

CC